Front. Phys. China, 2007, 2(3): 289−311
DOI 10.1007/s11467-007-0049-9

REVIEW ARTICLE

LANG Xing-you, JIANG Qing

Size dependence of phase transition temperatures of ferromagnetic, ferroelectric and superconductive nanocrystals

Abstract With the miniaturization of devices, size and interface effects become increasingly important for the properties and performances of nanomaterials. Here, we present a thermodynamic approach to the mechanism behind size-induced unusual behavior in the phase stabilities of ferromagnetic (FM), antiferromagnetic (AFM), ferroelectric (FE), and superconductive (SC) nanocrystals, which are different dramatically from their bulk counterparts. This method is based on the Lindemann criterion for melting, Mott's expression for the vibrational melting entropy, and the Shi model for the size-dependent melting temperature. Simple and unified functions, without any adjustable parameter, are established for the size and interface dependences of thermal and phase stabilities of FM, AFM, FE and SC nanocrystals. According to these analytic functions, as the size of nanocrystals is reduced, the thermal and phase stabilities may strengthen or weaken, depending on the confluence of the surface/volume ratio of nanocrystals and the FM(AFM, FE or SC)/substrate interface situations. The validity of this model is confirmed by a large number of experimental results. This theory will be significant for the choice of materials and the design of devices for practical application.

Keywords thermodynamics, phase transition, nanocrystals, ferromagnet, antiferromagnet, ferroelectrics, superconductor

PACS numbers 05.70Fh, 05.70Jk, 61.46+w, 75.30.-m, 77.80.Bh, 74.78.-w

LANG Xing-you, JIANG Qing (✉)
Key Laboratory of Automobile Materials (Jilin University), Ministry of Education, and Department of Materials Science and Engineering, Jilin University, Changchun 130025, China
E-mail: jiangq@jlu.edu.cn

Received March 7, 2007

1 Introduction

1.1 Scope

This report starts with a brief overview on the unusual behavior of phase stabilities of ferromagnetic (FM), antiferromagnetic (AFM), ferroelectric (FE) and superconductive (SC) nanocrystals. A deeper and consistent insight into the mechanism behind the observations and determining factors dominate the general trends of the size-induced property change, which are of fundamentally great importance for advancing technological applications. Several recent models pursued for these size dependences are also comparatively discussed. In Section 2, a simple method is developed to establish a unified model, without any adjustable parameter, for the phase transition of nanocrystals. This model is based on Lindemann's criterion for melting [1], Mott's expression for the vibrational melting entropy [2], and Shi's model for the size-dependent melting temperature, with considerations of interface conditions and dimensions [3]. Section 3 develops this method to illustrate the size dependences of FM, AFM, FE and SC transition temperatures: The Curie temperature of FM and FE nanocrystals [$T_{cm}(D)$ and $T_{ce}(D)$], and the Néel temperature of AFM nanocrystals [$T_N(D)$], as well as the critical transition temperature of SC nanocrystals [$T_{cs}(D)$], where D denotes the size of nanocrystals: the diameter of nanoparticles and nanorods or nanowires, or the thickness of thin films. Comparisons of model predictions with available experimental evidence are also presented in the corresponding section. In addition, the relationships between this model and the previous functions are comparatively discussed in Section 3. Section 4 summarizes the main contributions and limitations of this work with suggestions for future directions in extending the developed knowledge and associated approaches.

1.2 Overview

The substances of low-dimensional nanocrystals can be compound, alloy, or elemental solids [4]. Nanocrystals with different dimension d (d = 0 for nanoparticles, d = 1 for nanorods or nanowires and d = 2 for thin films), bridge the gap between the isolated atoms and their bulk counterparts in terms of chemical, physical, and mechanical properties. In comparison with bulk counterparts, the key difference of nanocrystals is the involvement of a high portion of atomic coordination imperfection in the surface and interface skins, which leads to intrinsic size dependences in mechanical strength, thermal and phase stabilities, acoustic (lattice dynamics), photonics, electronics, magnetism, dielectrics, as well as chemical reactivity [4]. These fascinating physicochemical properties of nanomaterials and the wide possibilities of using these properties in practical applications have attracted great interest. The current progress in nanotechnology has made the fabrication of individual nanocrystals possible, which in turn provides an opportunity to study the basic properties of nanomaterials. In the previous years, following Takagi's pioneering work in 1954 [5] of experimentally demonstrating that ultrafine metallic nanocrystals melt below their corresponding bulk melting temperature, the thermal and phase stabilities of nanomaterials have been intensively studied experimentally and theoretically since they are of concern in the design of devices and choice of governing materials for practical applications. Simultaneously, the application of advanced theoretical methods and new computational tools can simulate and explain the corresponding phenomena [6].

In this report, special attention is paid to the most active fields in modern physics, the phase stabilities of low-dimensional FM [7–9], AFM [9], FE [10–12], and SC [13, 14] systems, of which the investigations are triggered by the occurrence of novel structures and phenomena, and by the perspectives and realization of a variety of technological applications. It is well known that low-dimensional FM, AFM, FE and SC nanocrystals possess unusual features, leading to new phenomena that are indeed surprising [7–14]. For instance, because of the breaking of lattice symmetry or surface dangling bond formation near and at the surface and interface, the structural and electronic properties are modified, which gives rise to site-specific surface anisotropy, surface spin disorder and weakened magnetic exchange coupling. As a consequence, intrinsic size dependences are brought out, which will be an advantage for functional sensors or switches.

1.2.1 FM and AFM nanocrystals

1.2.1.1 Ordering temperature of FM and AFM nanocrystals

The Curie temperature T_{cm} and the Néel temperature T_N are the most important properties to characterize FM and AFM phase stabilities. Size dependences of T_{cm} and T_N of a large number of low-dimensional FM and AFM systems have been investigated experimentally, such as nanoparticles, nanorods, thin films and multilayer systems. They consist of the magnetic transition metals Fe, Co, and Ni, as well as rare-earth metal films like Gd and Tb. Also, the alloys and compounds of these materials have been studied. Commonly, the monolayer or multilayer magnetic films are epitaxially grown on or between nonmagnetic materials like noble metals, nonmagnetic transition metals, semiconductors, insulators, or magnetic substrates.

Prominent examples are the Fe/SiO [15], Fe/Ag(001) [16], Fe/Au(100) [17], Fe/Pd(100) [18], Fe/Ag(111) [19], Fe/Ag(100) [20], Co/Cu(100) [21], Co/Cu(111) [22, 23], Co/Cu(001) [23, 24], Ni/Cu(100) [23], Ni/Cu(001) [24], Ni/Cu(111) [25], Ni/W(110) [26], Co_1Ni_1/Cu(100) [23], Co_1Ni_3/Cu(100) [23], Co_1Ni_9/Cu(100) [23], Gd/W(110) [27], Gd/W [28], Nb/Gd [29], and Gd/Y(0001) [30] systems, and other low-dimensional nanocrystals, i.e., Ni nanorods [31, 32] and nanoparticles [32, 33], Gd [34], Fe_3O_4 [35], and $MnFe_2O_4$ [36] nanoparticles. Interest in the thin films, superlattices, nanoparticles and nanorods of AFM insulators has grown for both fundamental studies and device application, as in the example of Ho/Nb/Y, Ho/Y/Nb [37], CoO/SiO_2 [38, 39], CoO/MgO [40], CoO/NiO [40], CoO/Fe_3O_4 [41], NiO/MgO [40,42] thin films and CuO nanoparticles [43–46] and nanorods [46].

The corresponding measurements have been performed by various means like magnetometry, the magneto-optical Kerr effect, ac-susceptometry experiments, ferromagnetic resonance, conversion-electron Mössbauer spectroscopy, X-ray magnetic circular dichroism, resonance magnetic X-ray spectroscopy, magnetic force microscopy, etc [9].

Generally, for free nanocrystals and thin films deposited on nonmagnetic substrates [15–40, 41–46], it has been found that $T_{cm}(D)$ and $T_N(D)$ functions are size-independent at D > 10 nm; as D is further reduced, $T_{cm}(D)$ and $T_N(D)$ decrease; finally, $T_{cm}(D)$ and $T_N(D)$ approach zero Kelvin for small-enough nanocrystals (usually a few monolayers) [15–36]. Furthermore, due to the different surface/volume ratio of free nanocrystals, the change of the $T_{cm}(D)$ function of nanorods or nanowires with D is weaker than that of nanoparticles [31–36, 43–46], but stronger than that of thin films [15–32, 37–40, 43–46]. Whereas, the $T_N(D)$ of CoO thin films supported by NiO and Fe_3O_4 substrates increases as D decreases [40, 41], which is attributed to the vicinity effect at the NiO/CoO and Fe_3O_4/CoO interfaces, where the exchange coupling of CoO is enhanced [40, 41]. This differs from the experimental results of Fe/Cr(001), where $T_N(D)$ decreases with dropping D [47], which could be induced by the spin-frustration effect in the vicinity of the rough Fe/Cr(001) interfaces, where the interfacial exchange energy can be minimized only locally and frustration of the interfacial spins occurs since Fe and Cr have magnetic long-range order [47].

Based on the aforementioned experimental data, numerous models have been proposed to understand the underlying mechanisms for $T_{cm}(D)$ and $T_N(D)$ functions. Among them, the pioneering theoretical work of Fisher and his co-workers strongly influences our general understanding [48], in which the spin-spin correlation length (SSCL) ξ is defined as the distance from a point beyond which there is no further correlation of a physical property associated with that point, and follows the temperature-dependent function $\xi(T) = \xi_0 t^{-\nu}$, where $t = 1-T/T_{cm}$ is the reduced temperature, ξ_0 is a microscopic length, and ν is a universal critical exponent [48]. According to this scaling relationship, $T_{cm}(D)$ is predicted to shift to a lower temperature than that of the bulk when ξ exceeds the film thickness. As far as thin films are concerned, the SSCL mechanism has given rise to a step function for $T_{cm}(D)$ with two adjustable parameters: One is ξ and the other is the exponent term $\lambda = 1/\nu$ [48, 49]. When $D > \xi$,

$$\frac{T_{cm}(D)}{T_{cm}(\infty)} = 1-\left(\frac{\xi + r_0}{2D}\right)^{\lambda} \tag{1a}$$

while when $D < \xi$,

$$\frac{T_{cm}(D)}{T_{cm}(\infty)} = \frac{D - r_0}{2\xi} \tag{1b}$$

where r_0 denotes the thickness of a monolayer, and ∞ denotes the bulk size.

Since nanoparticles have different characteristics of $T_{cm}(D)$ functions from that of thin films, further unified models are considered to suit these new cases. In light of the effect of the breaking of exchange bonds, the $T_{cm}(D)$ function of nanoparticles has been proposed as [50]:

$$\frac{T_{cm}(D)}{T_{cm}(\infty)} = 1-\frac{3\Delta L}{2D} \tag{2}$$

where ΔL is the thickness of the surface layer of nanoparticles, which characterizes the influence of the surface layer on the $T_{cm}(D)$ function of nanoparticles. However, when this model is utilized to fit experimental data on the $T_{cm}(D)$ function of Fe_3O_4 nanoparticles, a constant ΔL cannot satisfactorily describe this case in the full size range of nanosize [50].

Since the dimension of nanocrystals d significantly affects the $T_{cm}(D)$ function, while Eqs. (1) and (2) consider, respectively, the cases of $d = 2$ for thin films and $d = 0$ for particles, they exhibit different forms due to this reason. Recently, Sun has established a unified model to consider the effect of dimension on $T_{cm}(D)$ by incorporating the bond order-length-strength (BOLS) correlation mechanism into the Ising premise [35],

$$\frac{T_{cm}(D)}{T_{cm}(\infty)} = 1+\sum_{i\leqslant 3}\gamma_i\left(z_{ib}q_i^{-w}-1\right) \tag{3}$$

where $q_i = \dfrac{h_i}{h} = \dfrac{2}{1+e^{(12-z_i)/(8z_i)}}$ shows a coordination number (*CN*)-dependent reduction of atomic diameter (h), $z_{ib} = z_i/z_b$, with z_i and z_b being the coordinates with and without *CN* imperfection, respectively, and $\gamma_i = \tau h q_i/D$ is the portion of atoms in the i-th atomic layer from the surface compared to the total number of atoms of the entire solid, and $\tau = 1$, 2, 3 correspond to thin films, nanorods, and nanoparticles, respectively. The power index w is an indicator for the bond nature and is an adjustable parameter [35]. When $w \approx 1$, $T_{cm}(D)$ functions of free nanocrystals with different dimensions are predicted with good correspondence of experimental results, where $T_{cm}(D)$ drops as D decreases [35].

Since there is an adjustable parameter in Eq. (3), further efforts are made to develop a model without a free parameter. Based on the size-dependent cohesive energy function, a model for the $T_{cm}(D)$ of thin films has been given as [51]:

$$\frac{T_{cm}(D)}{T_{cm}(\infty)} = \left(1-\frac{1}{2D/ch-1}\right)e^{\frac{-2S_b}{3R}\Big/\left(\frac{2D}{ch}-1\right)} \tag{4}$$

where S_b is the bulk evaporation entropy of crystals, and R is the gas constant. c_1 is added as an additional condition for different surface states. $c_1 = 1$ for the nanocrystals with free surface where the potential of surface atoms of the nanocrystals differs from that of the interior of the nanocrystals. When the interface interaction between the nanocrystals and the corresponding substrate is weak, such as thin films deposited on inert substrates, the film/substrate interaction is of weak van der Waals forces while the inner interactions within the thin films are strong chemical bonds, $c_1 = 1/2$. If this strength on the interface is comparable with that within films, c_1 varies somewhat [51]. When these are similar, which is equal to the case that one of the two surfaces of the films disappears, $c_1 = 1/2$ is thus obtained (the side surfaces of the thin films are neglected due to the low thickness). For more complicated interfaces, c_1 may be considered case by case to be between 1/2 and 1. Eq. (4) has presented a qualitative explanation for the drop in the $T_{cm}(D)$ function of nanocrystals with the decrease of D.

In addition to Eqs. (1)–(4), another theoretical model (a finite-size scaling relationship [22, 23]) has also been proposed for reproducing $T_{cm}(D)$ functions of Co/Ni alloys:

$$\frac{T_{cm}(\infty)-T_{cm}(D)}{T_{cm}(D)} = \left(\frac{D-D'}{\xi_0}\right)^{-\lambda} \tag{5}$$

with D' denoting the finite thickness of films at $T_{cm}(D) = 0$. Although Eq. (5) can also fit the experimental data of Co, Co_1Ni_1, Co_1Ni_3 and $CoNi_9$ [22, 23], it strictly holds only in the large size limit of D with the help of three adjustable parameters D', ξ_0 and λ. Since these parameters are different case by case during matching of the experimental results when the experimental sources are different [22, 23], the physical meaning of these parameters is unclear.

In the explanations of $T_N(D)$ functions, besides the empirical law that is of similar form of Eq. (5) [9, 37], the finite-size scaling law has also been employed to analyze the experimental data [38]

$$\frac{T_N(D)}{T_N(\infty)} = 1-\left(\frac{\xi_0}{D}\right)^{\lambda} \tag{6}$$

and $\xi(T) = \xi_0[1-T/T_N(\infty)]^{-\nu}$, where ξ_0 is the extrapolated correlation length at $T = 0$ K [38].

1.2.1.2 Thermal stability in exchange-biased FM/AFM bilayers

Exchange bias refers to a shift of the hysteresis loop along a magnetic field axis, which can be observed in exchange-interacting FM/AFM materials [52]. Materials exhibiting the exchange bias and related effects have been proposed and utilized in applications, such as permanent magnet materials, high density recording media, domain stabilizers in recording heads, spin-valve devices and giant magnetoresistance (GMR) type devices [53–55]. However, the microscopic origin of this effect is not well understood yet [53–55].

One of the most important properties of exchange bias is its thermal stability, indicated by the blocking temperature T_b, which is of concern for the design of magnetic heads and governs the choice of the biasing materials [53–55]. At T_b, the exchange bias field H_e, which is equal to the shift of the hysteresis loop, approaches zero. T_b has been intensively investigated as a function of AFM layer thickness D due to its scientific and industrial importance. As D decreases, $T_b(D)$ functions have been indicated to decrease in the Fe_3O_4/CoO [41, 56, 57], NiO/NiFe [58], CoNiO/NiFe [58], IrMn/NiFe [58], Py/IrMn [59], NiFe/IrMn [60], CoFe/IrMn [61, 62], IrMn/NiFe [62], FeMn/NiFe [63], MnPt/CoFe [64] and FeF_2/Fe bilayer systems [65]. Empirical $T_b(D)$ functions have been proposed to fit the corresponding experimental data. One of them, based on the thermal fluctuation model for polycrystalline AFM films, has been given as follows [60, 66, 67]:

$$\frac{T_b(D)}{T_b(\infty)} = 1 - \left(\frac{\xi_1}{D}\right)^{\lambda} \tag{7}$$

where $\xi_1 = J_{INT}/(2K_{AFM}ra)$ corresponds to the correlation length and J_{INT} is the interface coupling exchange between the FM and AFM spins, K_{AFM} is the magnetic anisotropy constant, r and a are the grain size and the lattice constant of AFM [66, 67], respectively.

Eq. (7) can also be obtained by extending the finite-size scaling of the $T_N(D)$ function [41, 58, 64, 65, 68]. This extension is, however, in contradiction to the recent work [41], which suggests that the variation of $T_b(D)$ differs from that of $T_N(D)$. $T_N(D)$ could increase with decreasing D because of the proximity effect of the adjacent FM layer [41]. In addition, within the $T_b(D)$ function of FeF_2/Fe system, the extracted parameter $\lambda = 0.8$ in Eq. (7) is physically unclear, and is much smaller than λ =1.56 and 1.42 for AFM derived from the Ising and Heisenberg models, respectively [65]. Furthermore, Eq. (7) is valid only for larger D values. Therefore, to establish a unified model with clear physical parameters to describe the $T_b(D)$ function in the full size range is necessary.

1.2.2 FE nanocrystals

1.2.2.1 Spontaneous polarization and $T_{ce}(D)$ of FE nanocrystals

Ferroelectric crystals are characterized by a displacement of ions from their centrosymmetric positions. This displacement leads to a net dipole moment of the unit cell and to a spontaneous static polarization. With increasing temperature this polarization decreases until, at the ferroelectric phase-transition temperature, T_{ce}, the crystal undergoes a phase transition from the polarized ferroelectric phase to the non-polarized paraelectric phase [10].

Since its discovery in 1920 by Valasek [69], ferroelectricity has attracted considerable interest from a fundamental point of view due to its wide range of potential applications [70]. In view of the sustained trend towards further miniaturization of microelectronic devices, investigations of the scaling effects in ferroelectrics acquire great practical importance [11, 12, 71]. For such cooperative phenomena, a different degree of ordering is expected to occur near the surface or interface, leading to an intrinsic dependence on sample size [72].

It is well known that the physical properties of low- dimensional ferroelectric crystals significantly differ from those of bulk ferroelectrics due to the surface or size effect [72–82]. Some early experimental results showed that the surface spontaneous polarization was less than the bulk for free nanoparticles, nanorods, and thin films, or $T_{ce}(D) < T_{ce}(\infty)$ [72–76, 79, 81–83]. However, some recent experiments have demonstrated that substrates impart mechanically on ultrathin epitaxial thin films, and may thus affect their phase transition characteristics and the order of the transition [11, 71, 72, 74–78]. This is induced by the elastic interaction with the transformation strain, which may assist or obstruct the transformation, and thus raise or lower the values of $T_{ce}(D)$ accordingly [72, 73, 77–79, 84–87]. The mechanisms of the concerned phenomena may be regarded as an interface effect, i.e., the modification of polarization near the surface or interface —a possible cause of the suppression or enhancement of ferroelectricity in low-dimensional ferroelectric crystals.

So far, many theories have been developed to describe the surface and size effect of ferroelectrics, which include the Landau phenomenological theory [80, 85, 86, 88, 89] and the transverse Ising models [35, 90–92]. The former has been more fruitful. In the Landau phenomenological theory, the free energy expansion coefficients are assumed to be size-independent, and the extrapolation length δ is introduced to illustrate the difference between the surface and the interior. When $\delta > 0$, polarization is reduced at the surface and $T_{ce}(D) < T_{ce}(\infty)$; When $\delta < 0$, polarization is enhanced at the surface and $T_{ce}(D) > T_{ce}(\infty)$ [80, 89, 92]. In the transverse Ising model, two-spin interaction constant and tunneling frequency are modified near the surface, which conse-

quently leads to the size dependence of ferroelectric properties [35, 90, 91]. Recently, Sun *et al.* [35] and Yang *et al*. [51] have obtained $T_{ce}(D)$ functions by combining the BOLS correlation mechanism and the size-dependent cohesive energy with the Ising premise, respectively, which are of the same forms of Eqs. (3) and (4).

Besides, as an empirical equation,

$$\frac{T_{ce}(D)}{T_{ce}(\infty)} = 1 + \frac{A}{D} \tag{8}$$

is widely pursued [76, 82], where A is a material constant. In addition, based on our model for size-dependent melting temperature, the $T_{ce}(D)$ equation of the perovskite ferroelectric nanocrystals with a first-order transition has been given by [93],

$$\frac{T_{ce}(D)}{T_{ce}(\infty)} = e^{\frac{-2S_0}{3R}/\left(\frac{D}{D_0}-1\right)} \tag{9}$$

where S_0 denotes the transition entropy, D_0 is the critical particle size where the ferroelectric phase cannot exist or the Curie transition is absent [93].

However, these models can only describe part of the experimental results, respectively. For instance, although the phenomenological Landau model has illustrated the tendency of the $T_{ce}(D)$ function with decreasing D, it has not given any comparison with experimental results except for Zhong *et al.* [92]. In addition, the existence of several adjustable parameters in the related models leads to the difficult understanding of the physical natures of the related phenomena. For the transverse Ising models [35, 51], only the decreased $T_{ce}(D)$ functions with D have been predicted where the interface effect and dimension dependence are neglected, such as the difference of the $T_{ce}(D)$ functions of two-dimensional thin films, one-dimensional nanowires or nanorods, and zero-dimensional nanoparticles. In fact, both effects on $T_{ce}(D)$ functions still remain unexplored [93]. Thus, there is urgent need to provide a unified model for size, dimension and interface effects on the $T_{ce}(D)$ of low-dimensional ferroelectric materials.

1.2.3 SC nanocrystals

1.2.3.1 $T_{cs}(D)$ of SC nanocrystals

Since its discovery by Onnes in 1911, superconductivity has become one of the most active fields in condensed-matter physics. The microscopic explanation of superconductivity proposed by Bardeen, Cooper and Schrieffer (BCS) in 1957 [94] is one of the landmark achievements of 20th-century physics. In recent years, there has been much speculation about the properties of superconductive nanocrystals, especially the possibility of achieving higher T_{cs}. As one of the most important properties of superconductors, $T_{cs}(D)$ has attracted great interest in experiments and theories. A common trend of low-dimensional nanocrystals is that $T_{cs}(D)$ decreases continuously as D is reduced, which has been observed in the systems of MgB_2 [95, 96] and Nb [97] thin films, Bi [98] and Pb [98−101] granular thin films and nanoparticles. Whereas, the $T_{cs}(D)$ of Al thin films and nanoparticles is revealed to increase with dropping D [98, 102].

Early on, to model the decreasing $T_{cs}(D)$ function with D, several models were brought forward. For small metal particles at low temperature, the electronic energy levels are discrete with a mean level spacing of the Kubo gap [103], $\delta_k = 4E_F/(3n_e) \propto 1/V_p \propto D^{-3}$, where E_F is the bulk Fermi energy, n_e is the ratio of valence/conduction electrons and V_p is the volume of the nanoparticles. As pointed out by Anderson, superconductivity would not be possible when δ_k becomes large than the bulk band gap. Based on this suggestion, a theoretical model has been provided to illustrate the decreasing of $T_{cs}(D)$ for nanoparticles [98,104], which has been given by $\ln[T_{cs}(D)/T_{cs}(\infty)] = \sum[2/(2M+1)]\{\tanh[\pi^2(2M+1)k_B T_{cs}/\delta]-1\}$, where k_B is the Boltzmann constant, and M is the magnetic quantum number. However, this prediction is in disagreement with the $T_{cs}(D)$ suppression of Pb nanoparticles, which are embedded in the Al-Cu-V matrix [100]. Instead, $T_{cs}(D)$ can be matched by an empirical equation, $T_{cs}(D)/T_{cs}(\infty) = \exp(-B/D)$, where B is an adjustable parameter [100]. Recently, Sun *et al* and Yang *et al* also extended their previous models of Eqs. (3) and (4) to interpret the $T_{sc}(D)$ function of SC nanocrystals, respectively [35, 51], where the decreasing $T_{sc}(D)$ functions with dropping D are qualitatively presented in the literatures of [35] and [51], respectively.

To illustrate the tendency of $T_{cs}(D)$ to increase with decreasing D, the models were developed by considering the electron-phonon coupling strength in the surface region of SC nanocrystals, and have been used to interpret the results of several superconductors [105, 106].

However, the aforementioned models interpret only a part of the experimental results, or only the monotonously varying tendency of $T_{cs}(D)$ as D is reduced. The development of a unified and general model is urgently needed.

1.3 Challenge

In the past decades, an overwhelming contribution has been made to the development of nanotechnology by the advent of methods such as atomic imaging and manipulating, nanocrystalline synthesizing, functioning, and characterizing as well as structural patterning for device fabrication [107]. However, insight into the underlying mechanisms and factors that dominate the general trend of tunability remains in its infancy. Based on the experimental observations, although a number of corresponding models have been proposed to interpret the size dependences, all these models often correspond to only a single phenomenon. A unified model dealing with all the related phenomena is highly de-

sirable. This unification will certainly give rise to the comprehension of the interdependence among the phase stabilities of nanocrystals.

The main objective of this contribution is to firstly present a review of the phase transitions of FM, AFM, FE and SC nanocrystals, and then propose a thermodynamic approach to modeling the observed experimental results. On the basis of this method, a systematical analysis of the underlying mechanism of size dependences of nanocrystals is illustrated in the corresponding sections.

2 Principle

It is worth emphasizing that the termination of the lattice periodicity in the surface normal has two effects. One is the reduction of the coordination numbers (CNs) of surface atoms and the other is the creation of a surface potential barrier [4]. Both result in a large number of physical quantities [$Q_s(D)$] at the surfaces or interfaces of nanocrystals being different from the internal counterparts [$Q_v(D)$]. Based on the mean-field approximation, the physical quantity of nanocrystals [$Q(D)$] can be given as [3, 4]

$$Q(D) = Q_v(D) + [Q_s(D) - Q_v(D)]n_s/n \tag{10}$$

where the subscript s and v indicate the surface atoms and the atoms located within the nanocrystals, respectively, $n_s/n \propto 1/D$ is the ratio of the number of surface atoms (n_s) to the total atom number (n) of nanocrystals [3].

In light of the idea of Eq. (10), if the cooperative coupling between the surface region and the interior region is phenomenologically considered by taking the variation of $Q(D)$ to be dependent on the value of $Q(D)$ itself, a change in Q can give rise to

$$Q(x + \mathrm{d}x) - Q(x) = (\alpha - 1)Q(x)\mathrm{d}x \tag{11}$$

which is achieved by assuming that Q_s and Q_v are size-independent, and $\alpha = Q_s/Q_v \approx Q_s(\infty)/Q_v(\infty)$, $x = n_s/n_v = D_0/(D - D_0)$ with D_0 denoting the critical size at which all the atoms or molecules of low-dimensional nanocrystals are located on their surfaces. In terms of the definition of D_0 and the bulk boundary condition, two asymptotic limits should be satisfied, namely $Q(D)/Q(\infty) \to 0$, when $D \to D_0$, and $Q(D)/Q(\infty) \to 1$, when $D \to \infty$. Associated with these boundary conditions and integrating Eq. (11), it is easy to obtain

$$\frac{Q(D)}{Q(\infty)} = \mathrm{e}^{\frac{(\alpha-1)n_s}{n_v}} = \mathrm{e}^{\frac{\alpha-1}{D/D_0-1}} \tag{12}$$

For low-dimensional nanocrystals, D_0 is dependent on the dimension of nanocrystals d: $d = 0$ for nanoparticles, $d = 1$ for nanorods or nanowires, and $d = 2$ for thin films. In general, the dimension can be fractal [108]. For the nanoparticles, D has a usual meaning of diameter; for the nanorods or nanowires, D is taken as their diameter; for thin films, D denotes the thickness. D_0 is given by (i) $D_0 = 6h$ for $d = 0$ since $4\pi h(D_0/2)^2 = 4\pi(D_0/2)^3/3$; (ii) $D_0 = 4h$ for $d = 1$ since $2\pi h(D_0/2) = \pi(D_0/2)^2$; and (iii) $D_0 = 2h$ for $d = 2$ since $2h = 2(D_0/2)$. In short,

$$D_0 = 2(3 - d)h \tag{13}$$

2.1 Atomic vibrational instability

Along the consideration of melting based on Lindemann′s criterion [1], letting $Q(D)$ be the mean-square displacement $\sigma^2(D)$, one obtains the extension of Eq. (12) for atomic vibrational instability of nanocrystals [3], namely,

$$\frac{\sigma^2(D)}{\sigma^2(\infty)} = \mathrm{e}^{\frac{\alpha-1}{D/D_0-1}} \tag{14}$$

where all the quantities have the same meanings as that in Eq. (12).

Since the melting temperature $T_m(\infty)$ are usually higher than the bulk Debye temperature $\Theta_D(\infty)$, the high temperature approximation can be utilized [3,109], $\sigma^2(D,T) = F(D)T$, where $F(D)$ is the T-independent but size-dependent parameter, where T is the absolute temperature. Thus, at any T, $\sigma^2(D, T)/\sigma^2(\infty, T) = F(D)/F(\infty)$. When $T = T_m$, $F(D)/F(\infty) = \{\sigma^2[D,T_m(D)]/h^2\}/\{\sigma^2[\infty, T_m(\infty)]/h^2\}[T_m(\infty)/T_m(D)] = T_m(\infty)/T_m(D)$ in terms of Lindemann′s criterion. Note that in the above consideration, the size effect on h has been neglected, i.e. V_s or h is assumed to be a size-independent constant, namely, $\Delta V_s = V_s(\infty) - V_s(D) \approx 0$ or $\Delta h = h(\infty) - h(D) \approx 0$. It is known that $\Delta h/h = \Delta V_s/(3V_s) = 0.1$–$2.5\%$ when $D < 20$ nm and it is negligible when $D > 20$ nm. Thus, even when $D < 20$ nm, $[V_s(D)/V_s(\infty)]^{2/3} \approx 0.95$–$0.97$. According to Eq. (14) [3, 108],

$$\frac{T_m(D)}{T_m(\infty)} = \frac{\sigma^2(\infty)}{\sigma^2(D)} = \mathrm{e}^{\frac{-(\alpha-1)}{D/D_0-1}} \tag{15}$$

The modern form of Lindemann′s criterion [110] has been given by, $\Theta_D(\infty) = f[T_m(\infty)/(MV^{2/3})]^{1/2}$, where f denotes a fraction of the nearest-neighbor spacing at which melting occurs, M is the molecular weight, and V_m is the molar volume. Size dependence of the $\Theta_D(D)$ function of nanocrystals can be obtained as a generalization of the above relationship, i.e., $\Theta_D^2(D)/\Theta_D^2(\infty) = T_m(D)/T_m(\infty)$ [108, 111]. Substituting Eq. (15) into this equation yields [108]

$$\frac{T_m(D)}{T_m(\infty)} = \frac{\Theta_D^2(D)}{\Theta_D^2(\infty)} = \mathrm{e}^{\frac{-(\alpha-1)}{D/D_0-1}} \tag{16}$$

According to Eq. (16), if $\alpha > 1$, $T_m(D)$ and $\Theta_D^2(D)$ decrease with decreasing D; when $\alpha < 1$, $T_m(D)$ and $\Theta_D^2(D)$ increase with decreasing D. In Eq. (16), the smallest size of crystals is assumed to be $2D_0$ where half of the atoms of a crystal is located on the surface with $n_s/n_v = 1$. Thus, $T_m(2D_0) = T_m(\infty)\exp(1-\alpha)$, where both crystal and liquid have almost the same short-range order and their structure difference is minimal. As a result, melting disappears [112].

By considering the vibrational entropy of melting of

nanocrystals $S_{vib}(D)$, deduced by Mott's expression for $S_{vib}(\infty)$ [2], the parameter α in Eq. (16) has been determined by [113]

$$S_{vib}(D) = S_{vib}(\infty) - \frac{3R}{2} \cdot \frac{\alpha - 1}{D/D_0 - 1} \quad (17)$$

For a free-standing or a quasi-free-standing nanocrystal, $S_m(2D_0) \approx S_{vib}(2D_0) = 0$ is assumed for the smallest nanocrystal as stated above, which leads to [108, 113]

$$\alpha_s = 1 + \frac{2S_{vib}(\infty)}{3R} \quad (18)$$

As a rule, melting entropy $S_m(\infty)$ consists, at least, of three contributions: positional $S_{pos}(\infty)$, vibrational $S_{vib}(\infty)$ and electric $S_{el}(\infty)$ [114]:

$$S_m(\infty) = S_{vib}(\infty) + S_{pos}(\infty) + S_{el}(\infty) \quad (19)$$

The idea of $S_{pos}(\infty)$ of melting arises in connection with the positional disorder as a substance undergoes a transition from the solid state to the liquid state. The number of particle species naturally plays a primary role in the disordering process. In the case of simple solids, only two particle species are present: the atoms of the given substance and vacancies [114]. In this case, $S_{pos}(\infty)$ is given by [114]

$$S_{pos}(\infty) = -R(x_A \ln x_A + x_v \ln x_v) \quad (20)$$

where $x_A = 1/(1+\Delta V_m/V_m)$ and $x_v = 1 - x_A$ are the molar fractions of the host material and vacancies, respectively, and ΔV_m is the molar volume difference between the liquid and the crystal.

For metallic crystals, the type of chemical connection does not change during the melting transition. Thus, $S_{el}(\infty) \approx 0$ [114] and $S_{vib}(\infty) = S_m(\infty) - S_{pos}(\infty)$, or

$$S_{vib}(\infty) = S_m(\infty) + R(x_A \ln x_A + x_v \ln x_v) \quad (21a)$$

For semi-metals, $S_{el}(\infty) \neq 0$, and $S_{vib}(\infty)$ must be determined in a direct way, i.e., Mott's equation [2],

$$S_{vib}(\infty) = 3R \ln \frac{v_s}{v_l} = \frac{3}{2} R \ln \frac{\mu_s}{\mu_l} \quad (21b)$$

where v and μ denote the characteristic vibration frequency and the electrical conductivity, respectively. If the parameters in Eq. (21b) are unavailable, the following equation can also be employed as a first-order approximation [114]:

$$S_{vib}(\infty) = S_m(\infty) - R \quad (21c)$$

For semiconductors, the melting is accompanied by semiconductor-to-metallic transition and the elements or compounds suffer contraction rather than expansion in volume for most metals. Thus, $S_{el}(\infty)$ strongly contributes to $S_m(\infty)$, and $S_{pos}(\infty) \square S_{el}(\infty)$. $S_{pos}(\infty)$ is thus negligible as a first-order approximation [115]. Namely,

$$S_{vib}(\infty) = S_m(\infty) - S_{el}(\infty) \quad (21d)$$

Note that Eq. (21d) is invalid for some metallic mixing oxides such as Fe_3O_4, consisting of Fe_2O_3 + FeO, which undergoes semiconductor-to-metal transition due to the Fe^{2+} and Fe^{3+} ions order on the *B* sites at 122 K (The so called Verwey transition), while the melting temperature is far above the Verwey temperature [116].

2.2 The verification of the model

Eq. (16) has been widely utilized to predict the $T_m(D)$ and $\Theta_D(D)$ functions of nanocrystals with different chemical bonds, such as organic [113], metallic [117, 118], and semiconductor crystals [119]. Figs. 1 and 2 give the verification of Eq. (16), where the model predictions of $T_m(D)$ and $\Theta_D(D)$ functions are consistent with the experimental techniques and computer simulation results of Au, Al, In, Fe, Sn, Se, Cu and Co nanocrystals with different dimensions d = 0, 1, 2.

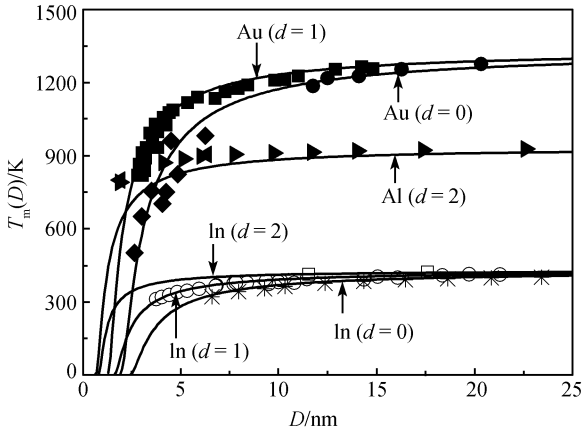

Fig. 1 Comparisons of $T_m(D)$ between model predictions according to Eq. (16) (*solid lines*) and available experimental evidence for Au, Al and In nanocrystals. The utilized parameters in the calculations are listed as follows: α = 1.621, 1.927, 1.609 in terms of Eq. (18) for Au, Al and In, respectively; in light of Eq. (13), D_0 = 1.154, 1.731 nm for Au nanorods (d = 1) and nanoparticles (d = 0), 0.6332 nm for Al films (d = 2), and 2.211, 1.474, 0.7368 nm for In nanoparticles (d = 0), nanorods (d = 1) and thin films (d = 2), respectively. The symbols ■ [117] and ●, ◆ [117] denote Au nanowires and nanoparticles, respectively; ► and ◄ [120] denote thin Al films; and ○□ and ∗ [121] denote In films, nanorods and nanoparticles. Other parameters are listed in Table 1.

Table 1 The parameters employed in the calculations of Eq. (16). $T_m(\infty)$ and $\Theta_D(D)$ are in K, $S_m(\infty)$ in J·g-atom^{-1}·K^{-1}, and h is in nm.

	$T_m(\infty)$ [131]	$\Theta_b(\infty)$ [118]	$S_{vib}(\infty)$ [118]	h [131]
Al	933.2		11.56	0.3166
Au	1337.3	184.6	7.74	0.2884
Co	1768.0	400.0	7.83	0.2507
Cu	1357.8	343.0	8.08	0.2556
Fe	1811.0	388.0	6.42	0.2482
In	429.8		7.59	0.3684
Se	494.0	135.9	10.93	0.4366
β-Sn	505.1	140.0	9.25	0.3181

As shown in these figures, the degree of variations of $T_m(D)$ and $\Theta_D(D)$ functions is strongly dependent on the dimension of nanocrystals, which is introduced by Eq. (13) with d = 0, 1 and 2 for the nanoparticles, the nanowires or nanorods and the thin films, respectively, while the computer simulation results are done with d = 0 [117, 122]. The

granular films cannot be described as a continuous film [108,118] since they are of high densities of inner surfaces or grain boundaries. This granular structure is similar to a random structure of a chain polymer modelled by a trajectory of a self-avoiding walk with a fractal dimension of $d' = (2 + d)/3$ [108,118]. For thin films, since $d = 2$, $d' = 4/3$ in terms of the above equation. This can be observed in Fig. 2, where $\Theta_D(D)$ functions (dashed lines) of Fe and β-Sn granular thin films are present, respectively.

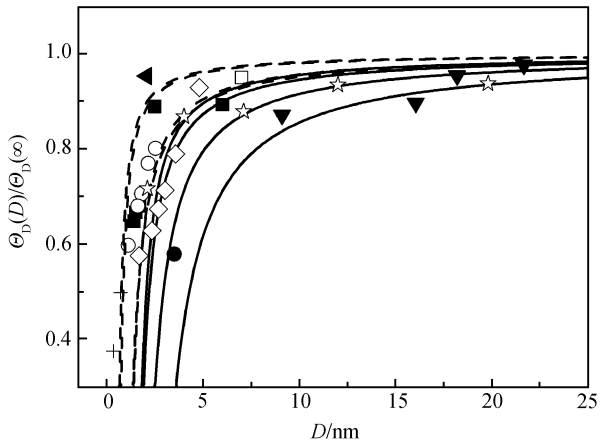

Fig. 2 Comparisons of $\Theta_D(D)/\Theta_D(\infty)$ between model predictions in terms of Eq. (16) and the available experimental results of Fe, Sn, Se, Cu, Co, Au nanocrystals, where the solid and dashed lines denote the prediction for nanoparticles and thin films, respectively. The parameters used in the calculations of Eq. (16) are listed as follows: α = 1.518, 1.742, 1.876, 1.648, 1.628, and 1.621 in light of Eq. (18) for Fe, Sn, Se, Cu, Co, and Au, respectively; According to Eq. (13), D_0 = 1.489, 0.4964 nm for Fe nanoparticles (d = 0) and thin films (d = 2), 1.908, 0.6362 nm for Sn nanoparticles (d = 0) and thin films (d = 2), 2.619 nm for Se nanoparticles (d = 0), 0.5112 nm for Cu thin films (d = 2), 1.505 Co nanoparticles (d = 0), and 0.5768 nm for Au thin films (d = 2). Other parameters are listed in Table 1. The symbols ■ [123], ○[124], +[125] denote Fe nanoparticles and thin films, respectively, ●[118] □[126] Sn films and nanoparticles, ▼ [127] Se nanoparticles, ◄ [128] thin Cu films, ◇[129] Co nanonparticles, ✯[130] Au films.

As shown in the above, the good agreements between model predictions and the experimental evidence confirm the validity of our model, which can predict the $T_m(D)$ and $\Theta_D(D)$ functions of low-dimensional nanocrystals with different dimensions.

3 Phase stabilities of FM, AFM, FE and SC nanocrystals

3.1 FM and AFM nanocrystals

3.1.1 Ordering temperatures of FM and AFM nanocrystals

In magnetic materials, the spins are coupled through strong, short-range exchange interactions and long-range magnetic dipolar interactions. It is well known that near the critical transition temperature, there exist two opposite forces: the ordering force due to the exchange interaction of magnetic moments, and the disordering force of lattice thermal vibrations. Based on the mean-field approximation [49,132],

$$k_B T_{cm}(\infty) = E_{exc}(\infty) \tag{22}$$

where E_{exc} is the spin-spin exchange interaction energy.

The average thermal vibrational energy is related to T by an equipartition relation of $m(2\pi\nu_E)^2\sigma^2(T) = k_B T$ [110], where m is the atomic mass, ν_E is the Einstein frequency. In terms of this relationship and Eq. (22), at $T_{cm}(\infty)$, the thermal vibration of atoms will destroy the magnetic ordering induced by the exchange interaction of nearest-neighbor atoms, $\sigma^2[T_{cm}(\infty)] = k_B T_{cm}(\infty)/[m(2\pi\nu_E)^2] = E_{exc}(\infty)/[m(2\pi\nu_E)^2]$. Similarly, based on Lindemann's basic assumption that melting occurs when σ reaches f at $T_m(\infty)$, $\sigma^2[T_m(\infty)] = k_B T_m(\infty)/[m(2\pi\nu_E)^2] = (fh)^2$ and $\Theta_D(\infty) = f\,[T_m(\infty)/(mh^2)]^{1/2}$ [110]. In terms of the above three relationships and an assumption that $E_{exc}(\infty)/(2\pi\nu_E f^2)^2 = K$ with K being a material constant, one can obtain [132]

$$T_{cm}(\infty) \propto \Theta_D^2(\infty) \tag{23}$$

If FM and AFM nanocrystals have the same crystal structure as the corresponding bulk, Eq. (23) can be extended to nanometer size, $T_{cm}(D) \propto \Theta_D^2(D)$. Thus, $T_{cm}(D)/T_{cm}(\infty) = \Theta_D^2(D)/\Theta_D^2(\infty)$. Substituting Eq. (16) into this equation leads to, $T_{cm}(D)/T_{cm}(\infty) = E_{exc}(D)/E_{exc}(\infty) = \exp[-(\alpha - 1)/(D/D_0 - 1)]$. The same case should occur for the $T_N(D)/T_N(\infty)$ function. Therefore [132],

$$\frac{T_{cm}(D)}{T_{cm}(\infty)} = T_N(D)/T_N(\infty) = \frac{E_{exc}(D)}{E_{exc}(\infty)} = e^{\frac{-(\alpha-1)}{D/D_0-1}} \tag{24}$$

For metallic or compound crystals with free surfaces, α_s is determined by Eq. (18). For FM or AFM films epitaxially grown on substrates, the effect of such epitaxial film/ substrate interfaces on α must be considered since the atomic vibration at the interface differs from that at free surfaces. Based on the Ising model, the simplest case is that only the surface and interface coupling constant (J_s and J_i) is different from the rest [133], where the subscript i denotes the interface. For the sake of simplicity, the effect induced by the exchange interface thickness is neglected while $J_i = J_s + J_{sub}$ is assumed as a first approximation with the subscript sub denoting the substrate. Thus, $\alpha_i = \sigma_i^2(D)/\sigma_v^2(D) = \alpha_s\sigma_i^2(D)/\sigma_s^2(D)$ in light of the definition of α where $\alpha_s = \sigma_s^2(D)/\sigma_v^2(D)$. Since the magnitude of the exchange interaction is proportional to the bond strength [56, 133, 134] while the bond strength is reversely proportional to σ^2 [134], $\sigma^2(D) \propto 1/J$. Thus, $\sigma_s^2(D) \propto 1/J_s$ and $\sigma_i^2(D) \propto 1/J_i$. As a consequence, $\sigma_i^2(D)/\sigma_s^2(D) = J_s/J_i$, or

$$\alpha_i = \alpha_s J_s / J_i \tag{25}$$

If the effects induced by surface and interface on $T_{cm}(D)$ and $T_N(D)$ are additive, according to Eq. (24),

$$\frac{T_{cm}(D)}{T_{cm}(\infty)} = \frac{T_N(D)}{T_N(\infty)} = \frac{1}{2}\left[e^{\frac{-(\alpha_s-1)}{D/D_0-1}} + e^{\frac{-(\alpha_i-1)}{D/D_0-1}}\right] \tag{26}$$

Note that Eq. (28) is only used for the case of thin films, while the side surface is neglected since the side surfaces have a small percentage of the total surface in comparison with that of the up surface and bottom interface of thin films. For nanoparticles and nanorods, the contribution of substrates on the order temperatures is neglected since the corresponding interface has only a small percentage of the total surface. In this case, Eq. (24) is directly used. In the following, although $T_{cm}(D)$ and $T_N(D)$ functions are denoted as Eq. (26), when the considered systems are nanoparticles and nanorods, $\alpha_s = \alpha_i$, and thus Eq. (26) = Eq. (24) [132].

3.1.2 *Verification: $T_{cm}(D)$ and $T_N(D)$ functions*

Figure 3(a)–(d) compare the model predictions of $T_{cm}(D)$ functions according to Eq. (26) with the available experimental measurements of magnetic transition metals and their alloys and compounds, such as Ni, Fe_3O_4 and $MnFe_2O_4$ nanoparticles, Ni nanorods, and Fe, Co, Co_1Ni_1, Co_1Ni_3, Co_1Ni_9, Ni thin films, which are deposited on a nonmagnetic metal substrates. For an epitaxial FM film on a magnetic inert substrate with negligible lattice mismatch, the exchange interac tion between them is assumed to be absent since it is assumed that the surface and the film/substrate interface are magnetically similar [37, 51, 132]. Thus, $\alpha_i = \alpha_s$ in terms of Eq. (25) with $J_i = J_s$ and $J_{sub} = 0$. On the other hand, for this kind of epitaxial films, the interaction strength at the film/substrate interface is comparable with the inner one [51], which results in the disappearance of one of the two surfaces of films. Thus, the critical size of the epitaxial films is $D_0/2$ [51, 132, 134].

As shown in this figure, the model predictions of Eq. (26) are quantitatively consistent with the experimental data of thin Fe, Co and Ni, CoNi alloy films epitaxially grown on silicon oxide glass [15], or nonmagnetic metallic substrates of Ag(001) [16], Au(100) [17], Pd(100) [18], Ag(111) [19], Ag(100) [20], Cu(100) [21], Cu(111) [22, 23], Cu(001) [23,

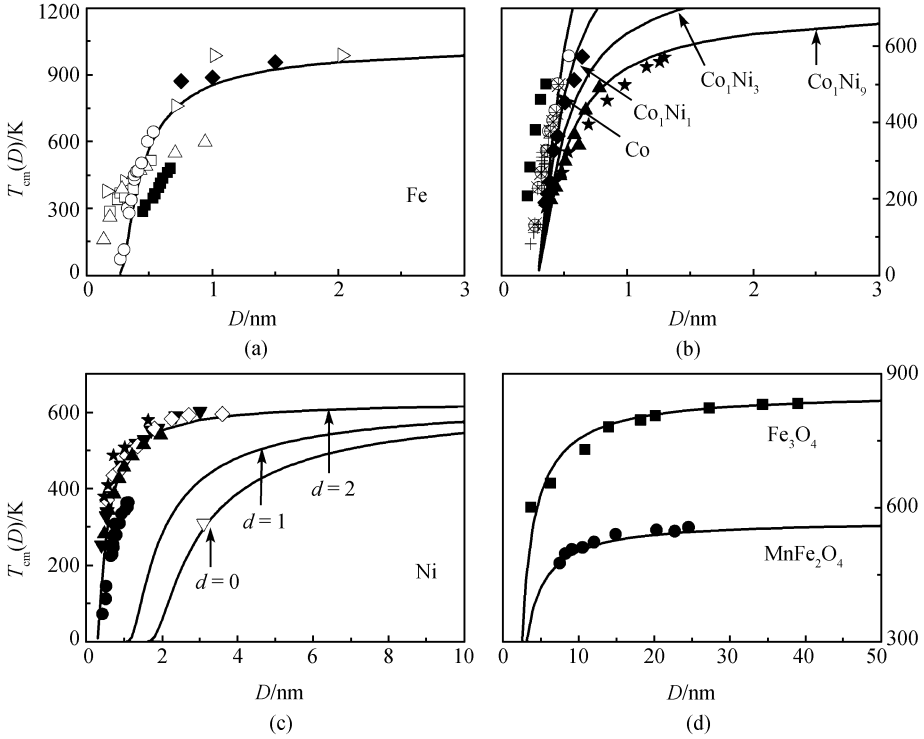

Fig. 3 Comparisons of $T_{cm}(D)$ functions between model predictions in light of Eq. (26) with available experimental measurements for Fe, Co, Co_1Ni_1, Co_1Ni_3, Co_1Ni_9, Ni, Fe_3O_4 and $MnFe_2O_4$ nanocrystals. The necessary parameters: **(a)** For Fe films, $D_0 = (2h)/2 = 0.2483$ nm in terms of Eq. (13) with $d = 2$, $\alpha_i = \alpha_s = 1.612$ according to Eqs. (18) and (25) with $J_s \approx J_i$, $J_{sub} \approx 0$, the symbols ◆ [15], ▷[16], □[17], ≥ [18], ● [19], and ■ [20] denote the experimental results of Fe/SiO, Fe/Ag(001), Fe/Au(100), Fe/Pd(100), Fe/Ag(111) and Fe/Ag(100) epitaxial films, respectively; **(b)** for Co, Co_1Ni_1, Co_1Ni_3 and Co_1Ni_9 alloy films, $D_0 = (2h)/2 = h = 0.2497$, 0.2495, 0.2493 and 0.2493 nm in terms of Eq. (13) with $d = 2$, and $\alpha_i = \alpha_s = 1.734$, 1.773, 1.792 and 1.803 according to Eqs. (18) and (25) with $J_s \approx J_i$, $J_{sub} \approx 0$, the symbols ○ [21], ∗ [22,23], ■ [23], + [24] denote the experimental evidences of Co/Cu(100), Co/Cu(111), Co/Cu(001) epitaxial films and ◆ [23], ▲[23] and ★ [23] denote the Co_1Ni_1/Cu(100), Co_1Ni_3/Cu(100), Co_1Ni_9/Cu(100) epitaxial thin films; **(c)** for Ni nanocrystals, D_0 = 1.4952, 0.9968, 0.2492 nm in term of Eq. (13) with $d = 0$, 1, 2, and $\alpha_s = 1.811$ in light of Eq. (18) for nanoparticles and nanorods, and $\alpha_i = \alpha_s = 1.811$ in terms of Eq. (25) with $J_s \approx J_i$ and $J_{sub} \approx 0$ for epitaxial films on inert substrates. The symbols ◆ [31], ∗ [32] denote Ni nanoparticles, ○ [32], ■ [33], ▽ [34] the nanorods, and ▲ [23], ● [24], ★ [24] ▼ [25], and ◇ [26] denote the experimental evidences of Ni/Cu(100), Ni/Cu(001), Ni/Cu(111), Ni/W(110) epitaxial films; **(d)** for Fe_3O_4 and $MnFe_2O_4$, D_0 = 1.338, 1.332 nm in terms of Eq. (13) with $d = 0$, and α_s = 1.8458, 1.8458 in terms of Eq. (18), the symbols ■ [35] and ● [36] denote Fe_3O_4 and $MnFe_2O_4$nanoparticles, respectively. The other necessary parameters used in the calculations are listed in Table 2.

Table 2 The parameters utilized in the calculations of Eq. (26) for FM materials. $T_{cm}(\infty)$ is in K, $S_m(\infty)$ in J·g-atom^{-1}·K^{-1}, and h is in nm.

	$T_{cm}(\infty)$ [51]	$S_m(\infty)$ [a]	h[d]
Fe	1043	7.628	0.2483
Co	1404	9.157	0.2497
Ni	630	10.12	0.2492
Gd	289	6.341	0.3575
Tb	230	6.626	0.3525
CoNi	1018	9.638 [b]	0.2495
Co_1Ni_3	824.3	9.879 [b]	0.2493
Co_1Ni_9	708.3	10.02 [b]	0.2493
Fe_3O_4	860	10.55	0.2220
$MnFe_2O_4$	573 [36]	10.55 [c]	0.2223

[a] The values of $S_m(\infty)$ refer to Ref. [131].

[b] $S_{m,Co_1Ni_n}(\infty) = [S_{m,Co}(\infty) + n S_{m,Ni}(\infty)]/(n+1)$ as a first approximation, where n denotes the number of Ni atoms in the compounds.

[c] Since no experimental data of $S_{m,MnFe_2O_4}(\infty)$ or $S_{vib,MnFe_2O_4}(\infty)$ are in hand, $S_{m,MnFe_2O_4}(\infty)$ is approximately equal to $S_{m,Fe_3O_4}(\infty)$.

[d] The values of h refer to Ref. [131] for elements and Refs. [35, 51] for compounds, respectively.

24]. It is well known that the depressed $T_{cm}(D)$ of FM nanocrystals should be attributed to the reduction in the number of spin interactions at the surface in comparison with that in the interior [49–51, 132]. The good agreement between Eq. (26) and the experimental data implies that the depression of $T_{cm}(D)$ of Fe Co and Ni, CoNi alloy epitaxial films on nonmagnetic metallic substrates should mainly be attributed to the effect of the free surface of nanocrystals [49–51,132]. Although Eqs. (1), (2) and (3) can also fit the experimental results of FM nanocrystals [35, 49–51], some adjustable parameters, such as ξ and λ in Eq. (1), ΔL in Eq. (2) and m in Eq. (3), are present. The utilization of these experimentally fitting parameters could mislead understanding of the related physical nature since the fitting parameters actually consist of several factors. It should be noted that for alloys the corresponding $T_{cm}(\infty)$ [51] and $S_m(\infty)$ [136] values are roughly estimated by their algebraic sum of elements. As shown in Fig. 3(b), Eq. (26) corresponds to experimental evidence well.

Figure 3(c) shows the comparisons of the $T_{cm}(D)$ function of Ni nanocrystals with different dimensions (d = 0, 1 and 2) between the experimental results and the predictions of this model. As seen in this figure, the $T_{cm}(D)$ function of low-dimensional Ni nanocrystals decreases with D. Furthermore, the change of the $T_{cm}(D)$ function of nanorods with D is weaker than that of nanoparticles, but stronger than that of thin films. These differences are induced by the different surface/volume (A/V) ratios of free nanocrystals since A/V = 6/D, 4/D and 2/D as d = 0, 1, 2, respectively [132]. Eq. (26) can describe this kind of changes induced by dimensions through introducing d values in Eq. (13). Since the freestanding materials have larger surface/volume ratio, their size dependences are stronger than that of the substances supported by substrates. However, this dimension effect has been neglected in Eqs. (1), (2) and (4).

In addition to the aforementioned metallic substances, the $T_{cm}(D)$ functions of compound nanocrystals such as Fe_3O_4 [35] and $MnFe_2O_4$ [36] nanoparticles are given in Fig. 3(d). As shown in the figure, the depressed $T_{cm}(D)$ of compound nanocrystals also follows Eq. (26) as D decreases in the full size range.

Figure 4 shows the comparisons of the $T_{cm}(D)$ functions of rare-earth metallic Gd and Tb nanocrystals between model predictions according to Eq. (26) and the experimental data. The wide distribution of the $T_{cm}(D)$ of Gd nanocrystals indicates that the $T_{cm}(D)$ of Gd is strongly dependent on the film's morphology [30], as well as on the lattice misfit between Gd film and the substrate [27]. For simplicity, these factors are neglected in this model, which does not bring out a big error.

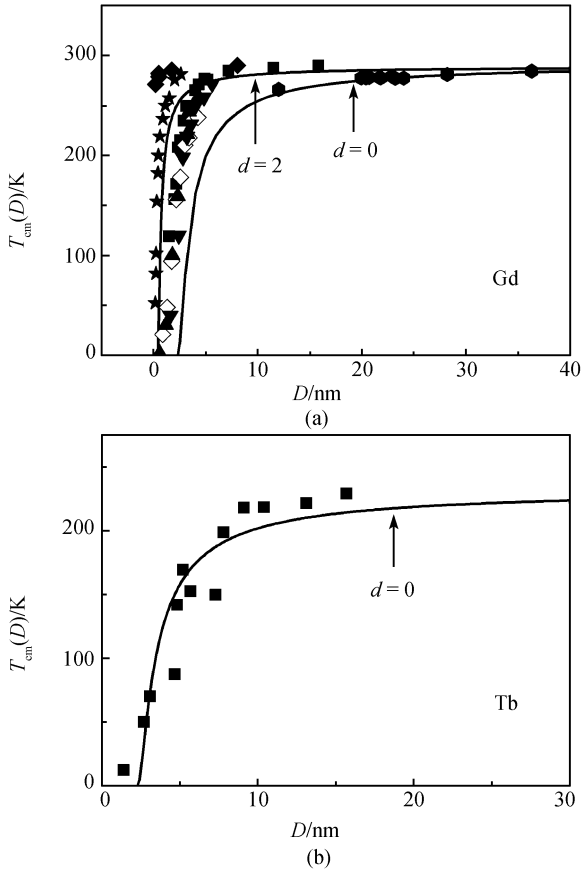

Fig. 4 Comparisons of $T_{cm}(D)$ functions between the model predictions in terms of Eq. (26) and available experimental results for **(a)** Gd nanoparticles and thin films, and **(b)** Tb nanoparticles. The necessary parameters: **(a)** D_0 = 2.145, 0.3575 nm according to Eq. (13) with d = 0, 2 for Gd nanoparticles and thin films, respectively, and α_s = 1.508 in terms of Eq. (18), $\alpha_i = \alpha_s$ = 1.508 in terms of Eq. (25) with $J_s \approx J_i$ and $J_{sub} \approx 0$ for epitaxial films on magnetic inert substrates, the symbols ■ [27], ◆ [27], ◇ [28], ▼ [29], ▲[29], ★[30] denote the experimental measurements of Gd/W(110), Gd/W, Nb/Gd and Gd/Y(0001) epitaxial films; ⬟ [34] denotes Gd nanoparticles; **(b)** D_0 = 2.115 nm according to Eq. (13) with d = 0 for Tb nanoparticles, and α_s = 1.531 in terms of Eq. (18), The symbol ■ [135] denotes Tb nanoparticles. Other parameters used for the calculations are listed in Table 2.

Based on the idea above, $T_N(D)$ should have a form similar to that of the $T_{cm}(D)$ function. The good agreements between the model predictions of $T_N(D)$ functions according to Eq. (26) and the available experimental evidence of Ho [37] and NiO [40, 42] thin films, CuO nanoparticles [43–46] and nanorods [46] are shown in Fig. 5(a) in the full size range.

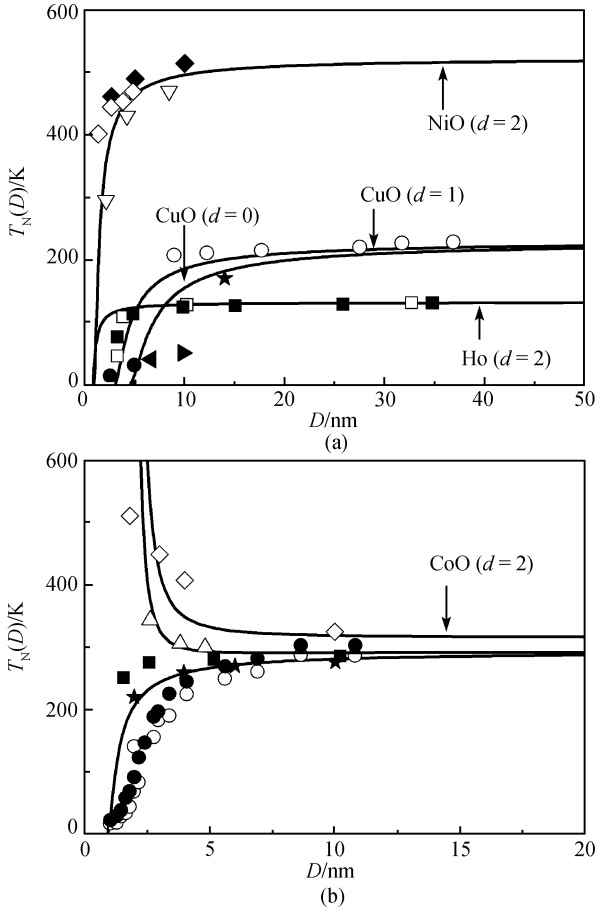

Fig. 5 Comparisons between model predictions of $T_N(D)$ functions in light of Eq. (26) and available experimental evidence: **(a)** NiO films (◆, ◇[40] and ▽ [42]), CuO nanoparticles (○[43], ◀ [44], ★[45] and ▶ [46]) and nanorods (●[46]), Ho thin films (■and □ [37]) and **(b)** CoO thin films epitaxially grown on SiO_2 or MgO substrates (●and ○ [40], ■and ★[38, 39]), and on Fe_3O_4 (△ [41]) and NiO (◇[40]) substrates, respectively. In light of the properties of the magnetic exchange interaction of AFM, the nearest spacing of the parallel spin-spin coupling of AFM $h = 2a$ with a being the lattice parameter since the lattice of AFM can be considered to consist of two sublattices with opposite spin direction [137]. **(a)** The parameters D_0 = 2.738, 4.107 nm for CuO nanorods and nanoparticles in terms of Eq. (13) with d = 0, 1, and $D_0 = (2h)/2 = h$ = 0.7154, 0.8420 nm for Ho and NiO thin films with d = 2, respectively, and α_s = 1.563 for CuO in terms of Eq. (18) and $\alpha_i = \alpha_s$ = 1.561, 1.583 for Ho and NiO thin films in terms of Eq. (25) with $J_s \approx J_i$ and $J_{sub} \approx 0$ for epitaxial films on inert substrates; **(b)** For CoO deposited on nonmagnetic substrates, the parameters $D_0 = (2h)/2 = h$ = 0.8520 nm in terms of Eq. (13) with d = 2, and α_i = 1.544 according to Eq. (25) with $J_s \approx J_i$, $J_{sub} \approx 0$ and α_s = 1.544 in terms of Eq. (13); for CoO supported by Fe_3O_4 and NiO substrates, α_i = 0.4139 and 0.5544 in terms of Eq. (25) with $\alpha_s J_s/(J_s+J_{sub}) \approx \alpha_s T_{cm}(\infty)/[T_{cm}(\infty)+T_{cm,sub}(\infty)]$, which is achieved based on the mean-field approximation, $J_s \propto T_{cm}(\infty)$ and $J_{sub} \propto T_{cm,sub}(\infty)$ or $J_s \propto T_N(\infty)$ and $J_{sub} \propto T_{N,sub}(\infty)$. Calculation parameters used are listed in Table 3.

Table 3 The parameters utilized in the calculations of Eq. (26) for AFM materials. $T_N(\infty)$ is in K, $S_m(\infty)$ in J·g-atom^{-1}·K^{-1}, and h is in nm.

	$T_N(\infty)$	$S_m(\infty)$ [b]	h
Ho	131.2 [37]	6.999 [131]	0.7154 [131]
NiO	523 [40]	7.271	0.8420 [40]
CoO	315 [38], 293 [40]	6.789	0.8520 [38, 40]
CuO	229 [46]	7.016	0.6845 [46]

[a] $S_m(\infty)$ of metallic oxides are given as $S_{m,MO}(\infty) = [S_{m,M}(\infty)+S_{m,O}(\infty)]/2$ as a first approximation since no experimental data are found, where the subscripts M and O denote the metal and oxygen atoms, respectively.

Similar results for CoO thin films epitaxially grown on SiO_2 or MgO substrate [38–40] have been shown in Fig. 5(b). Whereas, for CoO thin films supported by Fe_3O_4 and NiO substrates, there exist strong exchange couplings at the CoO/Fe_3O_4 or CoO/NiO interface where the thermal vibration of interface atoms is suppressed and much higher energy is required to disorder the ordering force [40, 41]. Therefore, $T_N(D)$ increases as D decreases. The predicted results of Eq. (26) are qualitatively consistent with experimental evidence. Note that other previous models have not considered this kind of cases [35, 49–51]. Although the free surface of such CoO film has still a tendency to lower the value of $T_N(D)$ of films, the total effect of the free surface and the interface leads to the drop in the total energy, and thus the increase of the $T_N(D)$ function with decreasing D. Furthermore, the stronger the interaction at the interface is, the more the $T_N(D)$ function increases [40, 41]. Thus, different substrates lead to the distinct values of $T_N(D)$ and $T_N(\infty)$ of CoO. For the sake of simplicity, the exchange bias effect from the FM/AFM interface, the existence of easy and hard axes, and magnetocrystalline anisotropy are neglected.

Considering the mathematical relationship of $\exp(-x) \approx 1-x$ when x is small enough as a first-order approximation, under the condition that $D \gg D_0$, Eq. (26) can be simplified as

$$\frac{T_{cm}(D)}{T_{cm}(\infty)} = \frac{T_N(D)}{T_N(\infty)} \approx 1-(\alpha_s+\alpha_i-2)\frac{D_0}{2D} \tag{27}$$

Comparing Eq. (27) with the scaling law of Eq. (1a) for thin films with $D > \xi$, $T_{cm}(D)$ follows a power law curve with λ = 1 [49]. Thus, Eq. (1a) can be rewritten as $T_{cm}(D)/T_{cm}(\infty) = T_N(D)/T_N(\infty) = 1-[(\xi + r_0)/(2D)]$ [49]. Associated with this relationship and Eq. (27), $\xi = (\alpha_s+\alpha_i-2)D_0-r_0$. For Fe, Co, Ni thin films, ξ = 0.4048, 0.5531, 0.6322 nm, respectively, which are approximately consistent with experimental and theoretical values of 0.4583, 0.3962, 0.7048 [49].

It is evident that Eq. (27) has a similar form to that of Eq. (2) for nanoparticles. Combining Eqs. (2) and (27),

$$\Delta L \approx 2(\alpha_s-1)D_0/3 \tag{28}$$

which indicates that ΔL is related to two parameters of S_{vib} and h. Substituting these parameters into Eq. (28), ΔL = 0.8084, 0.9692, 0.7521, 0.7512 and 1.541 nm for Ni, Gd, $MnFe_2O_4$, Fe_3O_4 and CuO nanoparticles, respectively, namely, $\Delta L \approx 3h$. Thus, when D is larger than several nanometers, Eq. (2) can be rewritten as,

$$\frac{T_{cm}(D)}{T_{cm}(\infty)}=\frac{T_N(D)}{T_N(\infty)}\approx 1-\frac{9h}{2D} \tag{29}$$

Eq. (29) becomes a pure geometrical equation and emphasizes the surface contribution on the $T_{cm}(D)$ function.

In light of Eqs. (3) and (27),

$$\sum_{i\leqslant 3} q_i(z_{ib}q_i^{-w}-1)\approx -(\alpha_s+\alpha_i-2) \tag{30}$$

Obviously, w is a function of materials, as well as interface conditions, which has been taken as an adjustable material constant in Eq. (3). According to Eq. (30), $\sum_{i\leqslant 3} q_i(z_{ib}q_i^{-w}-1)=0.0421$ for the case of CoO epitaxial films on Fe_3O_4 substrates. With this value, the $T_N(D)$ function of Eq. (3) is predicted to increase as D is reduced, which is qualitatively consistent with the experimental evidence.

Compared with the previous models [35, 49–51], this unified model without any adjustable parameter can be utilized to predict the effects of dimension and interface on the $T_{cm}(D)$ or $T_N(D)$ function through the introduction of the parameter D_0 and α, respectively. When $0<\alpha<1$, $T_{cm}(D)$ or $T_N(D)$ increases with decreasing D, while the opposite occurs when $\alpha>1$, which is determined by the common effects of both the surface and film/substrate interface with different interface interaction strengths. Furthermore, when Eq. (27) is reasonable, the adjustable parameters appearing in Eqs. (1)–(3) could be quantitatively determined and a more exact physical meaning of these parameters may be found.

3.1.3 Dependence of $T_b(D)$ in exchange-biased FM/AFM bilayers on the thickness of the AFM layer

For an exchange-biased FM/AFM system comprising a thick FM layer with a thickness of t_{FM} and an AFM layer with infinite thickness, $D\rightarrow\infty$, the magnitude of the exchange bias field at 0 K, $H_{e0}(\infty)$, is related to the FM/AFM interfacial energy, $E_0(\infty)$, where $H_{e0}(\infty)=E_0(\infty)/(M_{FM}t_{FM})$ [53–55]. In this relationship, M_{FM} is the fixed saturation magnetization of the FM layer because the effect of t_{FM} on H_e is assumed to be constant in this situation. To estimate the value of $H_{e0}(\infty)$, two theoretical approaches have been pursued to determine the value of $E_0(\infty)$. On the basis of the idea of planar domain walls at a smooth FM/AFM interface, $E_0(\infty)$ can be given by $E_0(\infty)=2[A_{AFM}(\infty)K_{AFM}(\infty)]^{1/2}$ [53–55, 138], where $A_{AFM}(\infty)=2J_{AFM}(\infty)S^2/a$ is the exchange stiffness [139], with J_{AFM} being the exchange integral and S the S-spin of AFM. The other theory argued that the assumption of an ideal interface was unrealistic, and the roughness of the interface leads to magnetic defects, which gives rise to local random fields [140]. Therefore, $E_0(\infty)$ was determined by, $E_0(\infty)=2z[A_{AFM}(\infty)K_{AFM}(\infty)]^{1/2}/\pi^2$ [53–55, 140], with z being a number of order unity. A common characteristic of both deductions is $E_0(\infty)\propto[J_{AFM}(\infty)S^2K_{AFM}(\infty)]^{1/2}$. According to this relationship and the mean field approximation [137], $J_{AFM}(\infty)S^2\propto E_{exc,AFM}(\infty)$, and thus,

$$E_0(\infty)\propto[E_{exc,AFM}(\infty)K_{AFM}(\infty)]^{1/2} \tag{31}$$

where $E_{exc,AFM}(\infty)$ denotes the spin-spin exchange interaction on the sublattice of AFM.

It is understandable that with increasing T the thermal energy $E_v(T)$ is introduced to decrease the FM/AFM interfacial energy, namely, $E_T(\infty)=E_0(\infty)-E_v(T)$, where $E_v(T)=k_BT$ in light of the Einstein′s relationship. At $T_b(\infty)$, taking $E_{T_b}(\infty)=0$ as reference, in terms of Eq. (31),

$$k_BT_b(\infty)\propto[E_{exc,AFM}(\infty)K_{AFM}(\infty)]^{1/2} \tag{32}$$

If the AFM nanocrystals have the same crystalline structure as that of the corresponding bulks, and the domain walls of the AFM layer are perpendicular to the FM/AFM interface [59, 66, 67, 141], $T_b(D)$ can be obtained as a generalization of Eq. (32), i.e., $k_BT_b(D)\propto[E_{exc,AFM}(D)K_{AFM}(D)]^{1/2}$. Combining this relationship and Eq. (32) brings out [142]

$$\frac{T_b(D)}{T_b(\infty)}=\left[\frac{E_{exc,AFM}(D)K_{AFM}(D)}{E_{exc,AFM}(\infty)K_{AFM}(\infty)}\right]^{1/2} \tag{33}$$

where $K_{AFM}(D)/K_{AFM}(\infty)=E_{exc,AFM}(D)/E_{exc,AFM}(\infty)$ is assumed if the size dependence of $K_{AFM}(D)$ is induced mainly by the size-dependent exchange anisotropy $E_{exca}(D)$ for the coherent FM/AFM interface [9]. Therefore, Eq. (33) can be rewritten as

$$\frac{T_b(D)}{T_b(\infty)}=\frac{E_{exc,AFM}(D)}{E_{exc,AFM}(\infty)} \tag{34}$$

For coherent FM/AFM structures, the $T_b(D)$ function is dependent not only on the FM/AFM interface interaction strength but also on the AFM field. The former determines the magnitudes of $T_b(\infty)$ [58–61], and the latter determines the size dependence of the $T_b(D)$ function. Since we consider only the relative difference of $T_b(D)$ and $T_b(\infty)$, while the value of $T_b(\infty)$ is taken directly from experiments, the contribution of the FM/AFM interface interaction strength to $T_b(\infty)$ is ignored. Based on this consideration and the mean-field approximation for AFM with sublattice magnetization [137], in terms of Eqs. (24) and (34) [142],

$$\frac{T_b(D)}{T_b(\infty)}=e^{\frac{-2S_{vib}(\infty)}{3R(D/2a-1)}} \tag{35}$$

3.1.3.1 Verification of $T_b(D)$

The comparisons of $T_b(D)$ functions between model predictions according to Eq. (35) and the available experimental data of Fe_3O_4/CoO [41, 56, 57], NiO/NiFe [58], CoNiO/NiFe [58], IrMn/NiFe [58], Py/IrMn [59], NiFe/IrMn [60], CoFe/IrMn [61, 62], IrMn/NiFe [62], FeMn/NiFe [63], MnPt/CoFe [64] and FeF_2/Fe bilayer systems [65] are shown in Fig. 6(a)–(c), where $T_b(D)$ functions decrease to zero Kelvin as D is reduced from bulk to thin-enough AFM layers (usually a few nanometers) [53–55]. The model predic-

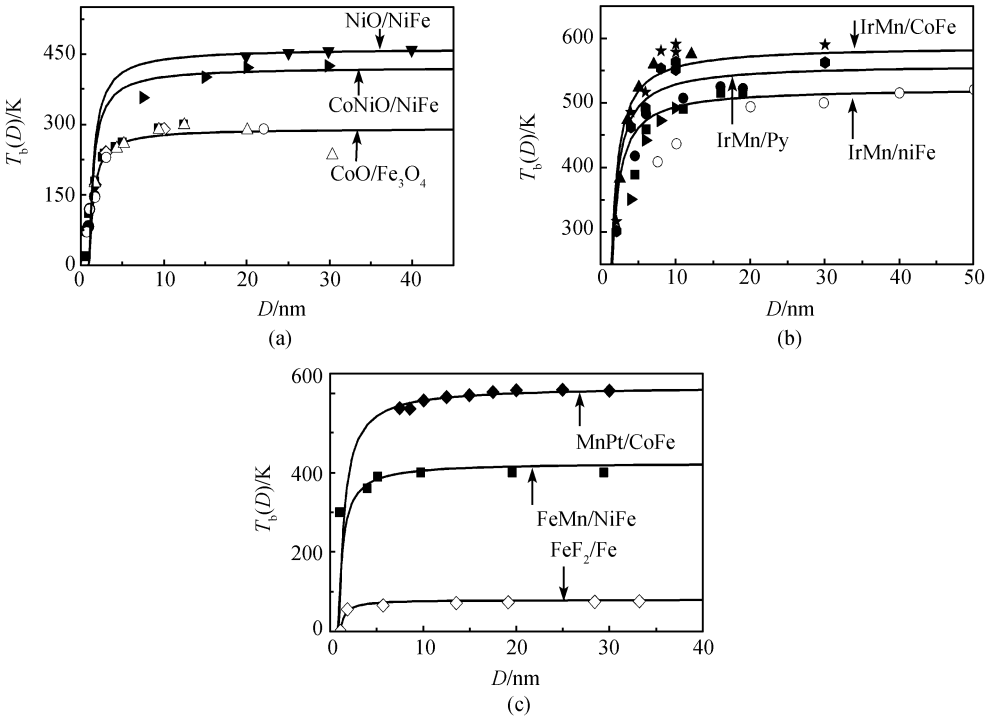

Fig. 6 Comparisons of $T_b(D)$ functions between model predictions in light of Eq. (35) with available experimental evidence: **(a)** Fe_3O_4/CoO (■[41], ◆ [41], ●[41], ▲[41], ○[56], △[56], ◇[57]), NiO/NiFe (▼ [58]) and CoNiO/NiFe bilayers (► [58]); **(b)** IrMn/NiFe (○ [58], ▲[60], ⬣ [62]) Py/IrMn (●, ■ [59]) and CoFe/IrMn bilayers (★ [61], ► [62]); **(c)** FeMn/NiFe (■ [63]), MnPt/CoFe (◆ [64]) and FeF_2/Fe bilayers systems (●[65]). The necessary parameters are listed in Table 4.

Table 4 Parameters utilized in calculations using Eq. (35) for the AFM materials. $T_b(\infty)$ is in K, $S_{vib}(\infty)$ is in J·g-atom^{-1}·K^{-1}, D_0 and ξ are in nm.

	$T_b(\infty)$	$S_{vib}(\infty)$[a]	$2a$[b]	ξ	δ[60]
CoO	292 [53]	6.789 [131]	0.8520	1.80 [38]	1.20
NiO	463 [58]	7.271 [131]	0.8420	1.92 [58]	1.40
CoNiO	423 [58]	7.899 [131]	0.8470	2.17 [58]	1.65
IrMn	523 [58],588 [61],560 [62]	8.776	0.7520	3.01 [58]	1.52
FeMn	425 [63]	7.786	0.7140	1.00 [65]	1.60
MnPt	616 [64]	8.764	0.7736	2.48 [66]	1.62
FeF_2	79 [65]	5.724	0.9380	0.73 [67]	0.62

[a] For alloys AB, $S_{vib}(\infty) = [S_{A,vib}(\infty)+S_{B,vib}(\infty)]/2$, where A and B denote different metallic atoms, and $S_{vib}(\infty)$ = 7.493, 7.628, 9.609, 9.584 J·g-atom^{-1}·K^{-1} for Mn, Fe, Ir, Pt [131], respectively.

[b] a = 0.4260 [57], 0.4210 [57], 0.3760 [142], 0.3570 [142], 0.3868 [142] and 0.4690 nm [142] for CoO, NiO, MnIr, FeMn, MnPt and FeF_2, respectively. D_0 = 0.4235 nm for CoNiO is the mean value of CoO and NiO.

tions agree quantitatively with the experimental evidence. It should be noted that the value of the $T_b(\infty)$ of IrMn comes from the corresponding experimental systems (IrMn/NiFe [58, 60, 62], Py/IrMn [59], CoFe/IrMn [61, 62]) for better fits with the model predictions, while many experimental factors affect $T_b(\infty)$ [53–55], such as anisotropy, stoichiometry or the presence of multiple phases, and the roughness at AFM/FM interfaces [53–55]. This stress is given because our contribution of Eq. (35) is to predict the relative difference of $T_b(D)$ and $T_b(\infty)$, not $T_b(\infty)$ itself.

According to the definition of T_b, it is natural to consider that T_b should be (at least slightly) below T_N and should depend on the strength of the FM/AFM interface exchange field [53–55]. This results from the unidirectional exchange anisotropy and the spin-spin exchange interaction of AFM with sublattice magnetization. It is well known that $T_b(D)$ corresponds to the situation at which the AFM spins follow the motion of the FM layer. Thus, $H_{eTb}(D) = 0$ because the unidirectional exchange anisotropy energy is smaller than E_0 [53–55], where $H_{eTb}(D)$ denotes the exchange bias at $T_b(D)$. This differs from the finite-size scaling of the $T_N(D)$ of AFM in the FM/AFM system, where J_{AFM} at the FM/AFM interface is enhanced, which results in the increase of the $T_N(D)$ function with the decrease of D [41, 65, 132].

Eq. (35) also sheds light on the $H_{e0}(D)$ function in the following form:

$$\frac{H_{e0}(D)}{H_{e0}(\infty)} = \frac{T_b(D)}{T_b(\infty)} = e^{\frac{-2S_{vib}(\infty)}{3R/2a-1}} \tag{36}$$

where the effect of the FM layers is set as an invariable. Both $H_{e0}(D)$ and $T_b(D)$ functions have the same trend with decreasing D. In terms of Eq. (36), the prediction of the $H_{e0}(D)$ function is presented in Fig. 7. As shown in the figure, the $H_{e0}(D)$ function decreases with decreasing D. The results qualitatively correspond to available experimental evidence with large scatters [56, 141, 143]. Note that since their $S_{vib}(\infty)$ values, in a size around the ideal gas constant, are similar (although the substances are different), the curves based on Eq. (36) are almost the same.

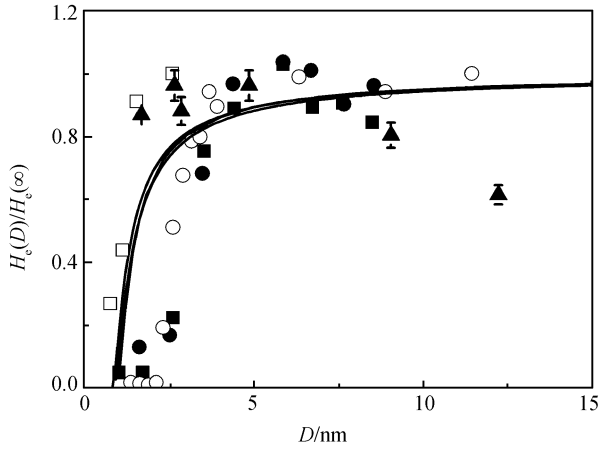

Fig. 7 Comparisons of $H_e(D)$ functions between model predictions in terms of Eq. (36) and available experimental results: CoO/Fe_3O_4 (□ and ▲ [56]), IrMn/NiFe (○[141]), FeMn/FeNi bilayers (■ and ● [143]). The utilized parameters are listed in Table 4.

Since there exists different degrees of spin-spin interactions between the inner and surface atoms because of the reduction in the number of spin interactions at the AFM surface [49], the $E_{exc,AFM}(D)$ function decreases with dropping D [49, 132]. Thus, the decreasing $T_b(D)$ and $H_{e0}(D)$ functions should be attributed to the decreasing exchange interaction field of the AFM layer with D [132, 142] because both $T_b(D)$ and $H_{e0}(D)$ functions are influenced by AFM layers. As shown in Figs. 6 and 7, although the related compounds show different spin structures, for example FeMn and MnPt have the non-collinear spin structure and the collinear spin structure, respectively, the model predictions of $T_b(D)$ and $H_{e0}(D)$ in light of Eqs. (35) and (36) are still in agreement with the experimental data, respectively.

3.1.3.2 Discussion on $\delta(D)$ and ξ functions

Following a mathematical relation of $\exp(-x) \approx 1-x$ when x is small enough, Eq. (35) can be simplified as

$$\frac{T_b(D)}{T_b(\infty)} \approx 1-\frac{C}{D} \tag{37}$$

where $C = 4aS_{vib}(\infty)/(3R)$. Eq. (37) indicates that the most important size effect on $T_b(D)$ relates closely to the surface/volume ratio of the AFM layer, or $1/D$ when $D > 10a \approx$ 7–8 nm.

Comparing Eq. (37) with Eq. (7), $\delta(D) = \{\ln[4aS_{vib}(\infty)/(3R)] - \ln D\}/(\ln \xi - \ln D)$. As $D \to \infty$, $\delta(\infty) = 1$. Thus,

$$\frac{\delta(D)}{\delta(\infty)} = \left[\ln\frac{4aS_{vib}(\infty)}{3R} - \ln D\right]/(\ln\xi - \ln D) \tag{38}$$

It is known that $\delta(D)$ in Eq. (7) depends on the non- universal value of the actual coupling strength in ultrathin films [27, 107, 109, 145], while the $\delta(D)$ function in Eq. (38) further indicates that this dependence is related to ξ. ξ at the FM/AFM interface results from the balance between the anisotropy energy of AFM and the FM-AFM spins' exchange coupling energy, $\xi \propto J_{INT}/K_{AFM}$ [60, 67]. In the mean-field theory, a similar relationship can be given as, $\xi_0 \propto J_{INT0}/K_{AFM0}$, with subscript 0 denoting the corresponding values of the mean-field approximation. As a result,

$$\frac{\xi}{\xi_0} = \frac{J_{INT}K_{AFM0}}{J_{INT0}K_{AFM}} \tag{39}$$

As $\xi = 4aS_{vib}(\infty)/(3R)$ for $D > 10a$ where Eq. (37) is valid, $\delta(D) = 1$ in terms of Eq. (38), which corresponds to the δ value of the mean-field theory and leads to $\xi_0 = 4aS_{vib}(\infty)/(3R)$ in terms of Eq. (7) [59, 142]. With a good approximation, $S_{vib}(\infty) \approx R$ for compounds and metallic atoms, and $a = \sqrt{2}\,h$ with h being the atomic diameter for face-centered cubic (fcc) structure, $\xi_0 \approx 4\sqrt{2}\,h/3$, which corresponds to the expected value of the FM/AFM exchange interface thickness restricted to $h \sim 2h$ [145, 146]. It should be mentioned that, ξ_0 is a little different for distinct crystalline structures of AFM since there exist different relationships between h and a for distinct crystal structures, such as $h = \sqrt{2}\,a/2$ and $h = (2a^2+c^2)^{1/2}/2$ for the NaCl structure and the body-centered tetragonal crystal structure, respectively.

Obviously, the experimentally overestimated J_{INT} value in comparison with J_{INT0} results in $\xi > \xi_0$ according to Eq. (39) while J_{INT} is strongly affected by experimental conditions, as listed in Table 4. In light of the ξ values of CoO, NiO, CoNiO, IrMn, FeMn and MnPt, the $\delta(D)$ function determined by Eq. (38) generally increases with decreasing D, which is shown in Fig. 8.

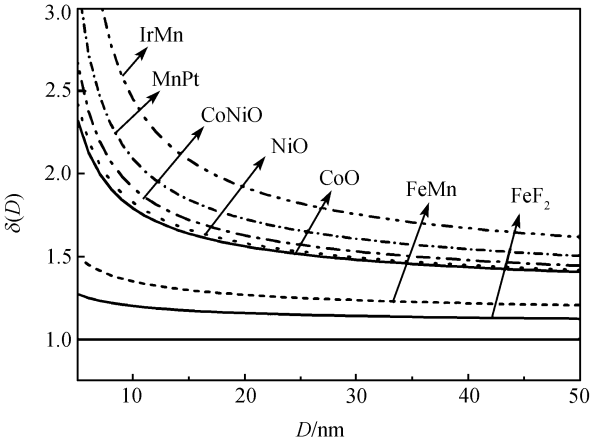

Fig. 8 Shift exponent $\delta(D)$ function in terms of Eq. (38) for CoO, NiO, CoNiO, IrMn, FeMn, MnPt and FeF_2 FM/AFM bilayers. The parameters used in the calculations of Eq. (38) are listed in Table 4.

If the J_{INT} value is derived from the Heisenberg model, where the spin-spin exchange coupling in thin films is assumed to be uniform throughout the films [137, 146], $J_{INT} > J_{INT0}$, $\xi > \xi_0$ and $\delta > 1$ [60] are also obtained since the exchange coupling near surfaces of thin films in mean-field approximation is expected to be weaker than that in the bulk [49, 142]. Nevertheless, for AFM materials with much

higher anisotropy, such as FeF_2 [65], ξ is predominantly determined by K_{AFM}, and the effect of J_{INT} is negligible. Thus, $\xi \approx \xi_0$ in terms of Eq. (39) with $J_{INT}/K_{AFM} \approx J_{INT0}/K_{AFM0}$, and $\delta(D) \approx 1$ with a very weak apparent size dependence according to Eq. (38).

If $\xi = \xi_0 = 4aS_{vib}(\infty)/(3R)$ and $\delta = 1$ in Eq. (7), Eq. (7) is the same as Eq. (38), in which the parameters are definitely physical in describing all $T_b(D)$ functions in the exchange-biased FM/AFM bilayers although Eqs. (7) and (38) are only valid for a thicker film limit. As $D \to h$, Eq. (35) is more suitable for predicting the $T_b(D)$ function since when D is comparable with h, energetic changes of internal atoms in AFM materials also contribute to T_b [142].

In light of the analysis above, the size dependences of the phase and thermal stabilities for low-dimensional FM and AFM nanocrystals and FM/AFM systems are still related with the surface/volume ratio, or $1/D$, which suggests a progressively increasing role of the surface layer with a decreasing D. As a key thermodynamic quantity, $S_{vib}(\infty)$ determines the atomic vibration and the interaction strength among atoms. This results in the interesting outcome that the phase and thermal stabilities of FM and AFM nanocrystals are also related to the natural properties of substances: S_{vib}, the size of nanocrystals and the corresponding bulk values that embody most of the properties of materials. In view of the relative difference between the values of bulk and nanocrystals being the emphasis in our model prediction, a simple and unified form can be obtained.

3.2 Displacive FE nanocrystals

3.2.1 Spontaneous polarization and ordering temperature of FE nanocrystals

From a fundamental point of view, the displacive ferroelectric materials characterized by macroscopic spontaneous polarizations P_s are caused by atomic off-center displacement, which results from a delicate balance between long-range (LR) Coulomb interaction and short-range (SR) covalent interaction [147]. It is well known that the ferroelectric properties in low dimensions are mainly determined by the truncation of long-range Coulomb interaction, which affects the dipoles located both at the surfaces and inside the materials and results in the alteration of P_s [80, 89, 92, 148]. As a particular case of tetragonal phase, P_s being normal to the surface ($P_x = P_y = 0$, $P_z = P_s \neq 0$, where the subscripts denote the polarization axis directions) is expected to be stable and the largest [72, 85, 149], which is typically the desired polarization direction in devices [150]. Now suppose that there exists a surface layer on the face of a low-dimensional ferroelectric nanocrystal with a size D, in which the surface spontaneous polarization $P_{ss}(D)$ differs from the interior one $P_{sv}(D)$. Letting the physical quantity Q in Eq. (12) be the spontaneous polarization P_s [151],

$$\frac{P_s(D)}{P_s(\infty)} = e^{\frac{\alpha-1}{D/D_0-1}} \tag{40}$$

where D_0 is determined by Eq. (13), in which h denotes the critical size of the basic structural unit required for ferroelectric activity at which $P_s = 0$ [151].

For freestanding perovskite ferroelectric nanosolids, the parameter α has been determined as [93, 151]

$$\alpha = \alpha_s = 1 - \frac{S_0(\infty)}{3R} \tag{41}$$

where the subscript s denotes the free surface.

The coupling effect between the mechanical deformation ε and P_s in the ferroelectric materials can be described via the electrostrictive coefficient Q_{ij}, namely, $\varepsilon = Q_{12}P_s^2$ with ε being the strain [85, 152, 153]. For thin perovskite ferroelectric films epitaxially grown on substrates, P_{si} at the interface can be expressed as, $Q_{12}P_{si}^2 = Q_{12}P_{sv}^2 + \varepsilon_i$, with $\varepsilon_i = (a_f' - a_f)/a_f$ and $Q_{12}P_{si}^2 \approx -|a_s - a|/a_s$, where $a_f' = a_f\{\beta(a_s - a)/[3a_s(s_{11} + s_{12})] + 1\}$ is the lattice constant of the tetragonal phase of the film under the stress $\sigma = (a_s - a)/[a_s(s_{11} + s_{12})]$ [85], where a_f and a are, respectively, the lattice constants of the tetragonal and cubic phase of ferroelectrics, β is the compressibility, a_s is the lattice constant of the substrate, and s_{11} and s_{12} are the elastic compliance constants. If some interface relaxation takes place, the real substrate lattice parameter a_s should be replaced by the effective substrate lattice parameter a_s^* [85, 154]. Based on the above relationships, in terms of the definition of α, let subscript i denote this interface, the corresponding $\alpha_i = P_{si}/P_{sv}$, namely [151],

$$\alpha_i = \left[1 - \frac{(a_f' - a_f)/a_f}{-|a_s - a|/a_s}\right]^{-1/2} \tag{42}$$

It should be noted that Eq. (42) has neglected the contribution of the strain gradients, which may be important in proper ferroelastics [149, 151], and the coupling between these gradients and polarization [149, 151].

Based on the effective-field theory developed to describe the lattice dynamics of ferroelectric systems, $T_{ce}(\infty) = kP_s^2(\infty)$ [155] with $k = \rho x \sum_b \frac{\gamma_b}{\lambda / k_B}$ where ρ is the parameter relating T_{ce} to ionic polarization $P_{ion}(\infty)$, x is the volume of a primitive cell in the crystal lattice, γ_b is a Lorentz-field tensor, and $\lambda = P_s^2(\infty)/P_{ion}^2(\infty)$. This relationship is valid over a wide range of materials [156]. From a simple physical consideration, this simple experimental and theoretical relationship may be interpreted as the equivalence between the lattice vibrational energy and the displacive energy of the ferroelectric state [156]. Note that here the influence of the depolarizing field is neglected because the remnant surface charge near the critical point is so small that the influence of the relevant depolarizing field becomes a secondary factor for structural instability [89]. If this relationship may be generalized for the corresponding size dependent function,

$T_{ce}(D)/T_{ce}(\infty) = P_s^2(D)/P_s^2(\infty)$. In terms of Eq. (40), the $T_{ce}(D)$ function of ferroelectric nanocrystals is established as

$$\frac{T_{ce}(D)}{T_{ce}(\infty)} = \frac{P_s^2(D)}{P_s^2(\infty)} = e^{\frac{2(\alpha-1)}{D/D_0-1}} \tag{43}$$

The existences of a free surface and substrate constraint destroy the macroscopic symmetry of the system and can significantly affect $T_{ce}(D)$. Under the assumption that the surface and interface effects on the $T_{ce}(D)$ is additive, thus [151],

$$\frac{T_{ce}(D)}{T_{ce}(\infty)} = \frac{P_s^2(D)}{P_s^2(\infty)} = \frac{1}{2}\left[e^{\frac{2(\alpha_s-1)}{D/D_0-1}} + e^{\frac{2(\alpha_i-1)}{D/D_0-1}}\right] \tag{44}$$

3.2.2 *Verification: $P_s(D)$ and $T_{ce}(D)$ functions*

According to Eq. (44), the $P_s(D)$ function (solid line) of $SrRuO_3/BaTiO_3/SrRuO_3$ capacitors is shown in Fig. 9, which strongly deviates from that of free $BaTiO_3$ films (denoted by the dashed line). This indicates that the $SrRuO_3/BaTiO_3$ interface not only results in the smaller critical size [151], but also takes a different role in impacting on the ferroelectric stability of films in comparison with that of free films. As shown in this figure, the good agreement between the model prediction and the available experimental measurements of $SrRuO_3/BaTiO_3/SrRuO_3$ layers [157] confirms the validity of this model.

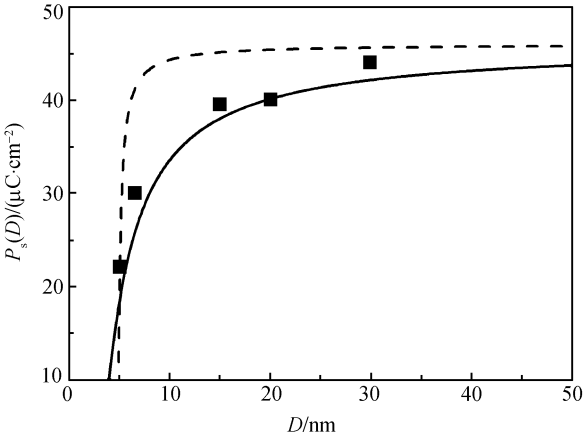

Fig. 9 Comparisons of the $P_s(D)$ function of $BaTiO_3$ thin films between model predictions according to Eq. (44) (*solid lines*) and the available experimental results of $SrRuO_3/BaTiO_3/SrRuO_3$ (■[157]). The necessary parameters are as follows: $\alpha_i \approx 0$ according to Eq. (42) since both $SrRuO_3$ and $BaTiO_3$ have approximately the same lattice constants [158], the critical size $D_0 = (2h)/2 = 2.4$ nm in terms of Eq. (15) with $d = 2$, and $P_s(\infty) = 46$ $\mu C\cdot cm^{-2}$ [157]. The dashed line denotes the $P_s(D)$ function of the free $BaTiO_3$ thin films, where $\alpha_s = 0.992$ in terms of Eq. (41) with $S_0(\infty) = 0.1$ $J\cdot g\text{-}atom^{-1}\cdot K^{-1}$ [93,151].

Figure 10(a) and (b) show the $T_{ce}(D)$ functions of the freestanding $BaTiO_3$ and $PbTiO_3$ nanocrystals ($d = 0$ for nanoparticles, $d = 1$ for nanorods or nanowires, $d = 2$ for thin films) according to Eq. (44). The main effect of a free surface is to alter the environment of the surrounding polarizable groups of atoms. This can result in the loss of translational invariance of the structure, and the modifications of the phonon spectrum and soft modes, as well as dipole-dipole interaction [71]. Therefore, it is reasonable to assume the existence of a surface layer of ferroelectric crystals in which the spontaneous polarization is lower than that of the interior [71, 80, 92], thus the suppression of $T_{ce}(D)$ is present. Similar to the $T_{cm}(D)$ functions of FM nanocrystals, as D is reduced, the change in the $T_{ce}(D)$ function of nanorods is also weaker than that of nanoparticles but stronger than that of thin films, which is induced by the different surface/volume ratios of freestanding nanosolids achieved through the introduction of a different dimension in Eq. (13) where $d = 2$, 1 and 0 for thin films, nanorods and nanoparticles, respectively.

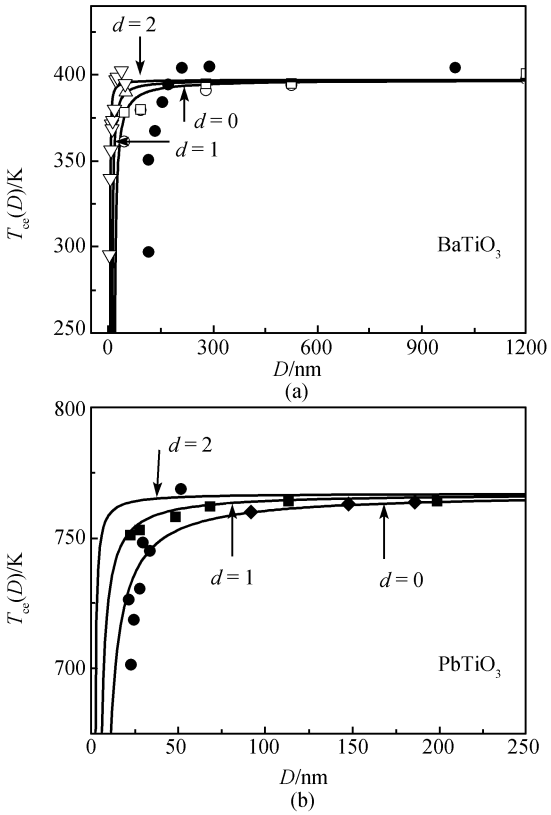

Fig. 10 Comparisons of $T_{ce}(D)$ functions between model predictions according to Eq. (44) and available experimental evidence for **(a)** $BaTiO_3$ and **(b)** $PbTiO_3$ free nanocrystals ($d = 0$ for nanoparticles, $d = 1$ for nanorods and $d = 2$ for thin films). The necessary parameters are as follows: **(a)** For $BaTiO_3$, $T_{ce}(\infty) = 397$ K [81], $\alpha_s = 0.992$ in terms of Eq. (41), $D_0 = 4.81$, 9.62, and 14.43 nm in light of Eq. (13) with $d = 2$, 1 and 0, respectively, and $h \approx 2.4$ nm [158]. The symbols ▲ [73], ●[93], ■ and ○[81], and ▽ [159] denote the available experimental results of $BaTiO_3$ nanoparticles and nanorods. **(b)** For $PbTiO_3$, $T_{ce}(\infty) = 769$ K is the average value of the corresponding experiments [151], $\alpha_s = 0.963$ in terms of Eq. (41) with $S_0 = 0.46$ $J\cdot g\text{-}atom^{-1}\cdot K^{-1}$ [93,151], $D_0 = 1.58$, 3.17 and 4.75 nm in terms of Eq. (13) with $d = 2$, 1 and 0, respectively, and $h \approx 0.8$ nm [72]. The symbols ◆ [74], ●[76], ■[82] denote available experimental results of $PbTiO_3$ nanoparticles.

The comparisons between the predicted $T_{ce}(D)$ functions in terms of Eq. (44) (solid line) and the available experimental evidences of $BaTiO_3$ and $PbTiO_3$ epitaxially grown thin films on different substrates are shown in Fig. 11(a) and (b), respectively. The model predictions correspond well to the available experimental evidence for the $BaTiO_3/SiO_2$ and $PbTiO_3/SrTiO_3$ systems. The dashed lines are the model predictions for the freestanding $BaTiO_3$ and $PbTiO_3$ thin films. As shown in Fig. 11(a) and (b), the tensile stress induced by the positive misfit strain ε_i at the coherent ferroelectrics/substrate interface will also result in the decrease of $T_{ce}(D)$ with D [71, 89]. Although this coherent interface brings out the disappearance of a free surface of the thin films, the tensile stress still constrains the ferroelectricity [71, 89]. Comparing with the $T_{ce}(D)$ function of the freestanding thin films with two free surfaces, the decrease of the $T_{ce}(D)$ of epitaxial thin films may be stronger or weaker. This is dependent on the magnitude of the misfit strain. As $\varepsilon_i > \varepsilon_v > 0$, the decrease of the $T_{ce}(D)$ of epitaxially grown thin films is stronger, which is shown in Fig. 11(a); while $0 < \varepsilon_i < \varepsilon_v$, the decrease of the $T_{ce}(D)$ of epitaxially grown thin films is weaker as shown in Fig. 11(b). This implies that when a tensile stress is applied, the ferroelectricity can be stabilized only in thicker films [89, 151].

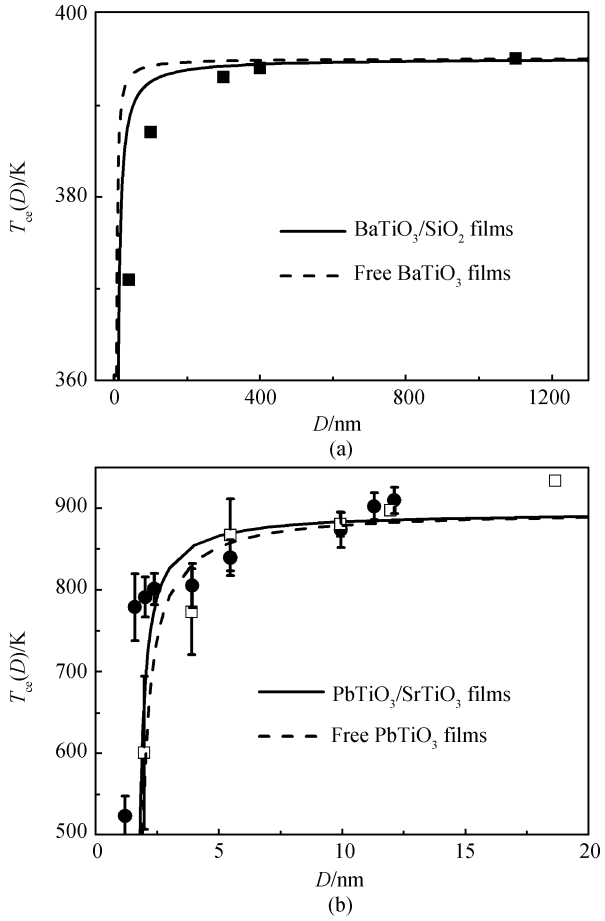

Fig. 11 Comparisons of $T_{ce}(D)$ functions between the model predictions of Eq. (44) for the $BaTiO_3$ and $PbTiO_3$ thin films epitaxially grown on different substrates (*solid lines*) and the available experimental evidence. The dashed lines are for the freestanding $BaTiO_3$ and $PbTiO_3$ thin films, respectively. **(a)** For the $BaTiO_3/SiO_2$ (■[79]) system with $T_{ce}(\infty) = 395$ K [79], the parameters are as follows: $\alpha_i = 0.8766$ for $BaTiO_3/SiO_2$ interface in terms of Eq. (42) with $a_s = 0.4179$ nm of SiO_2, respectively, and $\beta = 5.1\times10^{-3}$ GPa^{-1} [160], $a = 0.40096$ nm and $a_f = 0.40051$ nm, $s_{11}+s_{12} = 5.62\times10^{-12}$ m^{2}N^{-1} [85]. $D_0 = 4.81$ nm in terms of Eq. (13) with $d = 2$. **(b)** For the $PbTiO_3/SrTiO_3$ epitaxial thin films (□ [72] and ● [78]), where $\alpha_s = 0.892$ in terms of Eq. (41), $\alpha_i = 0.9838$ in terms of Eq. (42) with $a_s = 0.3905$ nm of $SrTiO_3$, and $\beta = 4.9\times10^{-3}$ GPa^{-1} [160], $a = 0.3905$ nm and $a_f = 0.3899$ nm [74], $s_{11}+s_{12} = 5.5\times10^{-12}$ m^{2}N^{-1} [85], $D_0 = 1.584$ nm in terms of Eq. (13) with $d = 2$, $T_{ce}(\infty) = 895$ K is The average value of the corresponding experiments [72, 85]. The other parameters are the same as that in Fig. 10.

Because of the electrostrictive coupling between lattice strain and polarization in ferroelectrics, the deformation of the lattice along the a_f and c_f tetragonal directions is proportional to P_s^2 [81]. Therefore, the tetragonal distortion η can be written, with good approximation, as $\eta(\infty) = (c_f - a_f)/a_f = (Q_{11}-Q_{12})P_s^2(\infty)$ [81]. If this relationship can be extended to nanometer size, in the light of Eq. (44), there is

$$\frac{\eta(D)}{\eta(\infty)} = \frac{P_s^2(D)}{P_s^2(\infty)} = \frac{T_{ce}(D)}{T_{ce}(\infty)} \tag{45}$$

which is obtained via the assumption that $Q_{11}-Q_{12}$ is size-independent. $\eta(D)$, $P_s^2(D)$ and $T_{ce}(D)$ have the same trends with the decreasing D.

The predictions of $T_{ce}(D)/T_{ce}(\infty)$ and $\eta(D)/\eta(\infty)$ functions are shown in Fig. 12 (a) and (b) for $BaTiO_3$/Pt(001)/MgO(100), $BaTiO_3/SrTiO_3$ systems, and the freestanding $PbTiO_3$ thin films and nanoparticles, respectively. The agreements between Eq. (45) and the experimental results imply that Eq. (45) is reasonable. Due to the compressive stress induced by the negative ε_i at the coherent $BaTiO_3$/Pt(001)/MgO(100) and $BaTiO_3/SrTiO_3$ interfaces, $\alpha_i > 1$ in terms of Eq. (42), which implies that this interface enhances the spontaneous polarization and tetragonality in favor of the stabilization of the ferroelectric phase [87,89,161]. Thus, $T_{ce}(D)$ and $\eta(D)$ functions increase with dropping D. In the calculation of Eq. (42), the parameter a_s of Pt(001) is replaced by the a_s^* because there exists a difference in the thermal expansion coefficient between Pt(001) and MgO(100), which results in the lattice relaxation of Pt(001) [85, 87, 154]. The $T_{ce}(D)$ functions of freestanding $PbTiO_3$ thin films and nanoparticles [in Fig. 12(b)] have similar results to that in Fig. 10(b).

Since the low-dimensional ferroelectric materials are particularly prone to processing-induced defects, which include microstructural heterogeneities, variations in crystalline quality, and mechanical stresses imposed on the materials by the substrates [71], the values of parameters in this model are taken from the corresponding experimental values for better correspondences.

Considering the mathematical relation of $\exp(x) \approx 1+x$ when x is small enough as a first-order approximation, Eq. (8) in fact is of the same form as that of Eq. (43), namely, $T_{ce}(D)/T_{ce}(\infty) \approx 1+2(\alpha-1)D_0/D$, which indicates that the most important size effect for low dimensional ferroelectric materials is still related with the surface/volume ratio, or $1/D$.

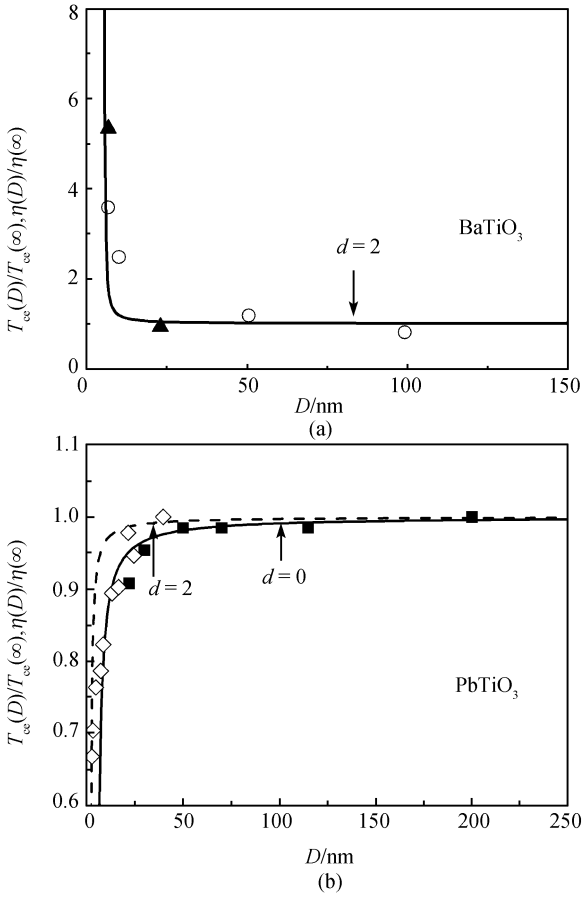

Fig. 12 **(a)** Comparisons of $T_{ce}(D)/T_{ce}(\infty)$ and $\eta(D)/\eta(\infty)$ between the predictions of Eqs. (44) and (45) and available experimental evidence for $BaTiO_3$ epitaxial thin films grown on Pt(001)/MgO(100) (○[87]) and $SrTiO_3$ (▲[87]), where $\alpha_1 \approx 1.1963$ according to Eq. (42) with $a_s = 0.3912$ nm of Pt(001) [87] for the $BaTiO_3$/Pt(001)/MgO(100) and $BaTiO_3$/$SrTiO_3$ interfaces. **(b)** Comparisons of $T_{ce}(D)/T_{ce}(\infty)$ between the predicted results in terms of Eqs. (44) and (45) (dashed line for the freestanding thin films, solid line for the nanoparticles) and available experimental results on the freestanding $PbTiO_3$ thin films (◇ [77]) and nanoparticles (■ [82]). The necessary parameters are the same as that of Figs. 10 and 11.

On the other hand, compared with the Landau phenomenological theory [89, 92] and the transverse Ising models [35, 90, 91], this model can be utilized to predict the effects of dimension and interface on the $T_{ce}(D)$ function without any adjustable parameter. Due to the surface lattice relaxation and the restraint from the lattice misfit between films and substrates, the order parameter of ferroelectrics P_s at the surface and the interface is introduced through the parameter α. When $\alpha < 1$, $T_{ce}(D)$ will increase with the decrease of D, while the opposite occurs when $\alpha > 1$, as shown in the above discussion. Although complicated, the size dependence of the Curie temperature of ferroelectrics can still be analyzed and predicted by this simple and unified model as long as the surface or interface conditions of the low-dimensional ferroelectric materials and relative thermodynamic parameters are clear.

3.3 SC nanocrystals

3.3.1 Ordering temperature of SC nanocrystals

According to the BCS theory of superconductivity [94], T_{cs} depends on the electron-phonon interaction in superconducting metals and compounds. Based on the theory, McMillan has deduced the following $T_{cs}(\infty)$ form [162], $T_{cs}(\infty) = [\Theta_D(\infty)/1.45]\cdot e^{\frac{-1.04(1+\phi)}{\phi-\mu^*(1+0.62\phi)}}$, where ϕ and μ^* are the electron-phonon coupling constant and the Coulomb pseudopotential of Morel and Anderson, respectively [162]. If $\mu^* \approx \phi$, this relationship can be approximated as [136]

$$T_{cs}(\infty) \propto \Theta_D(\infty) \tag{46}$$

It is assumed that $T_{cs}(D)$ has the same size dependence of $\Theta_D(D)$ [163], or

$$\frac{T_{cs}(D)}{T_{cs}(\infty)} = \frac{\Theta_D(D)}{\Theta_D(\infty)} \tag{47}$$

Substituting Eq. (16) into Eq. (47) leads to [136]

$$\frac{T_{cs}(D)}{T_{cs}(\infty)} = e^{\frac{-(\alpha-1)/2}{D/D_0-1}} \tag{48}$$

where the parameter α is determined by Eq. (18) for free nanocrystals. On the other hand, for metallic nanosolids with oxide at the surface such as Al [98,102,164], $\alpha < 1$ according to the definition of $\alpha = \sigma_s^2(D)/\sigma_v^2(D)$ [132, 134, 136] because the metal-oxygen bonding is stronger than metal-metal bonding. Under the assumption that the bond strength is inversely proportional to σ^2 [132, 134, 136], namely, $\sigma_s^2(D) \propto 1/E_s$ and $\sigma_v^2(D) \propto 1/E_v$, where E denotes the bond strength, the α in this case can be expressed as [136]

$$\alpha = \frac{E_v}{E_s} \tag{49}$$

3.3.2 Verification: $T_{cs}(D)$ function

The model predictions in terms of Eq. (48) and the available experimental data of Nb, Pb, Bi and MgB_2 thin films and nanoparticles are shown in Fig. 13(a)–(d), where good correspondences within the experimental error range are observed. As shown in the figures, $T_{cs}(D)$ decreases as D drops. It is observed at once that $D \to t_0$ where t_0 is the critical size where the superconductivity vanished and t_0 can be determined in terms of the Kubo formula [103], $T_{cs}(D)$ functions decrease dramatically although t_0 does not appear in Eq. (48). Note that, since Bi and Pb thin films may refer to finely granular structures with high densities of inner surfaces/grain boundaries and cannot be described by a continuous film [166], this granular structure is similar to a random structure of a chain polymer modelled by a trajec-

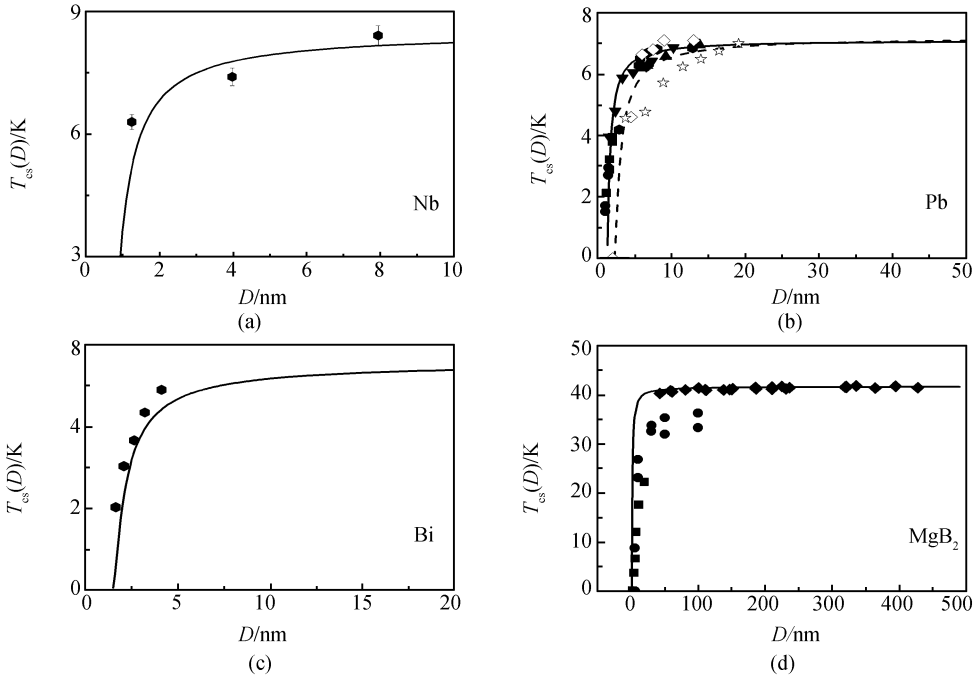

Fig. 13 Comparisons of $T_{cs}(D)$ functions between model predictions according to Eq. (48) and available experimental results for **(a)** Nb films (●[97]) **(b)** Pb nanoparticles (◇ [100], ★ [101]) and films (▲, ● , ▼ , ■ [98],● [99]), **(c)** Bi films (⬢[98]) and (d) MgB_2 films (■[35], ●[95], ◆ [96]). The necessary parameters are listed as: **(a)** for Nb, $T_{cs}(\infty) = 8.5$ K [97], $D_0 = 0.6512$ nm in terms of Eq. (13) with $d = 2$ and $h = 0.3256$ nm [131], $\alpha = 1.781$ in terms of Eq. (18) with $S_{vib} = S_m = 9.74$ J·mol^{-1}·K^{-1} [131]; **(b)** for Pb, $T_{cs}(\infty) = 7.2$ K [101], $D_0 = 1.3000$, 2.3400 nm in terms of Eq. (13) with $d = 4/3$ and $d = 0$ for granular films and nanoparticles, respectively, and $h = 0.3900$ nm [131], $\alpha = 1.6406$ in terms of Eq. (18) with $S_{vib} = S_m = 7.99$ J·mol^{-1}·K^{-1} [131]; **(c)** for Bi, the mean value $T_{cs}(\infty) = 5.57$ K since this value is located within the range of 2.60 – 8.55 K [165], $D_0 = 1.358$ nm in terms of Eq. (13) with $d = 4/3$ and $h = 0.4074$ nm [131], $\alpha = 1.9389$ in terms of Eq. (18), which is determined by substituting $S_{vib} = S_m - R = 11.71$ J·mol^{-1}·K^{-1} in terms of Eq. (21c) where $S_m = 20.02$ J·mol^{-1}·K^{-1} [131]; **(d)** for MgB_2, $T_{cs}(\infty) = 41.7$ K [35], $D_0 = 0.7084$ nm in terms of Eq. (13) with $d = 2$ and $h = 0.3490$ nm, since no experimental data for S_{vib} or S_m are in hand, $S_{vib} = 12.20$ J·mol^{-1}·K^{-1} is taken, which is obtained by mean values of S_{vib} of elements consisting of the compounds, namely $S_{vib}(MgB_2) = [S_{vib}(Mg)+2S_{vib}(B)]/3$ where $S_{vib}(Mg) = S_m(Mg) = 9.74$ J·mol^{-1}·K^{-1} [131], $S_{vib}(B) = S_m(B) - R = 13.43$ J·mol^{-1}·K^{-1} in the light of Eq. (21c) [131]. Substituting this value into Eq. (18), $\alpha = 1.9783$.

tory of a self-avoiding walk with a fractal dimension of $d' = (2+d)/3$ [108, 136]. For thin films, since $d = 2$, $d' = 4/3$ in terms of the above equation. This can be observed in Fig. 13(b) and (c) where the $T_{cs}(D)$ functions of Bi and Pb granular thin films are present, respectively.

The comparisons of enhanced $T_{cs}(D)$ between the model prediction in terms of Eq. (48) and available experimental evidence for Al thin films and Al nanoparticles is shown in Fig. 14 where α is determined by Eq. (49). The model prediction roughly corresponds to the experimental results in the experimental error range. This enhancement of the superconducting temperature is induced by the existence of alumina on the surface of Al nanosolids with Al-O bonding [102, 164], which leads to the vibrational suppression of surface Al atoms and thus $\alpha < 1$.

In Figs. 13(b) and 14, $T_{cs}(D)$ functions of nanoparticles are also predicted in terms of Eq. (48) by introducing dimension-dependent D_0 values determined by Eq. (13), where qualitative agreements between the predictions and experimental evidence are found. This extension in crystal shape from films to particles or rods is valid only when the crystal has a continuous, rather than discrete, electron spectrum

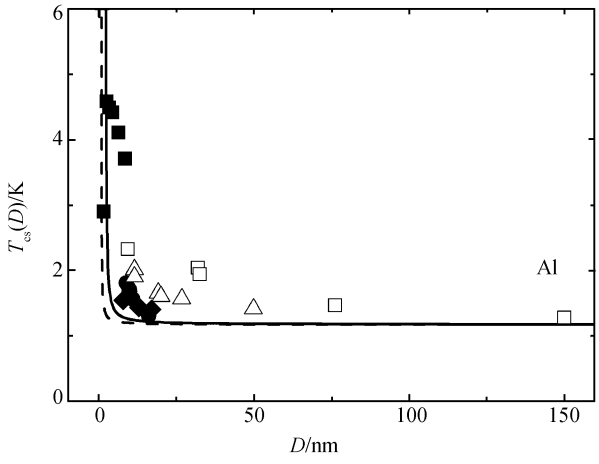

Fig. 14 Comparisons of $T_{cs}(D)$ of Al nanoparticles and thin films between model predictions according to Eq. (48) (*solid and dashed lines* for nanoparticles and for thin films, respectively) and available experimental measurements (■ [198] and ◆, ● [102] for nanoparticles, □, △ [136] for thin films). The parameters in Eq. (48) are as follows: $T_{cs}(\infty) = 1.175$ K [165], $D_0 = 1.8996$ nm or 0.6332 nm in terms of Eq. (13) for nanoparticles with $d = 0$ or for thin films with $d = 2$ where $h = 0.3166$ nm [131]. $\alpha = 0.3636$ in terms of Eq. (49) with $E_{Al\text{-}Al} = E_v = 186.2$ kJ·mol^{-1} [165] and $E_{Al\text{-}O} = E_s = 512.1$ kJ·mol^{-1} [165].

[167, 168], which, however, may be questionable for nanoparticles since the discreteness of the electron spectrum changes the effective electron density states and coupling strength [169, 170]. The deviations between Eq. (48) and the experimental evidence shown in Figs. 13(b) and 14 may indeed be attributed to this effect. Nevertheless, since superconductive thin films and nanoparticles have the similar forms of the external field dependence of energy gap [167], and if their surface atoms are assumed to have the same vibrational mode [136], the mechanisms of the superconducting transition of thin films could qualitatively be applied to nanoparticles without big error [167, 168].

For nanosolids, not only the electronic properties but also the phonon spectrum will certainly be influenced by size. Because of the favorable surface-to-volume ratio in nanosolids, it is also possible that electron-electron interaction will be influenced via surface phonons [136]. The two parameters Θ_D and σ describing the vibrational lattices or atoms are useful in determining the role of phonons in its superconducting mechanism. In light of modern field theory, an electron will have a self-energy in this vibrational field since it produces a lattice deformation that in turn reacts on the electron, which can be considered as the attractive interaction among the electrons. The interaction results in the lowering of the energy of the systems below the energy gap where these electrons are in long-range order, namely, in a superconducting state.

As shown in the figures, the complicated $T_{cs}(D)$ functions for SC nanocrystals can still be described in a simple and unified form as long as the related thermodynamic parameters of crystals are known. Eq. (48) affords more facilities for predicting $T_{cs}(D)$ with two parameters being dependent on material and structure.

4 Concluding remarks

On the basis of the thermodynamic method, several analytical models that are free of adjustable parameters are presented to quantitatively model the size and interface dependences of phase transition temperatures of FM, AFM, FE, and SC nanocrystals. The unified form of the functions not only reveals that the physical nature of size and interface dependences of material properties and critical transition temperatures should be attributed to the surface/volume ratio of nanocrystals, but also illustrates the underlying relationship between the thermal and phase stabilities. It is worth emphasizing that this method is to be used to predict the relative difference of nanocrystals and bulk counterparts, while most of the properties of the materials have been embodied in the bulk properties. Thus, our model prediction could be realized in a simple and unified form. The success of the above classic thermodynamics in the full size range of materials further enriches classical thermodynamic theory, as well as offers powerful, irreplaceable and unfailing theoretical guidance for the development of materials science.

However, since thermodynamics can only describe the statistical behavior of large numbers of molecules, this thermodynamic top-down method cannot be utilized to depict the action of clusters with only a few molecules or atoms. Once D decreases to D_0, the quantum effect is introduced, which results in the disability of this method. In addition, if the corresponding structure of nanocrystals differs from that of the corresponding bulk, where the electronic distribution varies, this model will be invalid since an important condition in this theory is that the nanocrystals are assumed to still have the same crystalline structure as bulk.

Because the present model is under the condition of single field, special attention in further works should be made on the improvement of this model for the multifield effect on the related properties of nanocrystals.

Acknowledgements The financial supports by the National Key Basic Research and Development Program (Grant No. 2004CB619301) and by the "985 Project" of Jilin University are acknowledged.

References

1. Lindemann F. A., Z. Phys., 1910,11: 609
2. Mott N. F., Proc. R. Soc. A, 1934, 146: 465
3. Shi F. G., J. Mater. Res., 1994, 9: 1307
4. Sun C. Q., Solid State Chem., 2007, 35: 1
5. Takagi M., J. Phys. Soc. Jpn, 1954, 9: 359
6. Raabe D., Computational Materials Science: The Simulation of materials Microstructures and Properties, New York: John Wiley& Sons, 1998
7. Bader S. D., Rev. Mod. Phys., 2006, 78: 1
8. Chien C. L., Annu. Rev. Mater. Sci., 1995, 25: 129
9. Jensen P. J., Surf. Sci. Rep., 2006, 61: 129
10. Bakker H. J., Hunsche S., and Kurz H., Rev. Mod. Phys., 1998, 70: 523
11. Ahn C. H., Rabe K. M., and Triscone J. M., Science, 2004, 303: 488
12. Dawber D., Rabe K. M., and Scott J. F., Rev. Mod. Phys., 2005, 77: 1083
13. Hilgenkamp H. and Mannhart J., Rev. Mod. Phys., 2002, 74: 485
14. Buzea C. and Yamashita T., Supercond. Sci. Tech., 2001, 14: R115
15. Lee E. L., Bolduc P. E., and Violet C. E., Phys. Rev. Lett., 1964, 13: 800
16. Stampanoni M., Vaterlaus A., Aeschlimann M., and Meier F., Phys. Rev. Lett., 1987, 59: 2483
17. Dürr W., Taborelli M., Paul O., Germar R., Gudat W., Pescia D., and Landolt M., Phys. Rev. Lett., 1989, 62: 206
18. Liu C. and Bader S. D., J. Appl. Phys., 1990, 67: 5758
19. Qiu Z. Q., Pearson J., and Bader S. D., Phys. Rev. Lett., 1991, 67: 1646
20. Qiu Z. Q., Pearson J., and Bader S. D., Phys. Rev. Lett., 1993, 70: 1006
21. Schneider C. M., Bressler P., Schuster P., and Kirschner J., Phys. Rev. Lett., 1990, 64: 1059
22. Huang F., Mankey G. J., Kief M. T., and Willis R. F., J. Appl. Phys., 1993, 73: 6760

23. Huang F., Kief M. T., Mankey G. J., and Willis R. F., Phys. Rev. B, 1994, 49: 3962
24. May F., Srivastava P., Farle M., Bovensiepen U., Wende H., Chauvistré R., and Baberschke K., J. Magn. Magn. Mater., 1998, 177–181: 1220
25. Ballentine C. A., Fink R. L., Araya-Pochet J., and Erskine J. L., Phys. Rev. B, 1990, 41: 2631
26. Li Y. and Baberschke K., Phys. Rev. Lett., 1992, 68: 1208
27. Farle M., Baberschke K., Stetter U., Aspelmeier A., and Gerhardter F., Phys. Rev. B, 1993, 47: 11571
28. Jiang J. S. and Chien C. L., J. Appl. Phys., 1996, 79: 5615
29. Jiang J. S., Davidović D., Reich D. H., and Chien C. L., Phys. Rev. Lett., 1995, 74: 314
30. Gajdzik M., Trappmann T., Sűrgers C., and Lőhneysen H. V., Phys. Rev. B, 1998, 57: 3525
31. Sun L., Searon P. C., and Chien C. L., Phys. Rev. B, 2000, 61: R6463
32. Cui X. F., Zhao M., and Jiang Q., Thin Solid Films, 2005, 472: 328
33. Du Y. W., Xu M. X., Wu J., Shi Y. B., Lu H. X., and Xue R. H., J. Appl. Phys., 1991, 70: 5903
34. Michels D., Krill III C. E., and Birringer R., J. Magn. Magn. Mater., 2002, 250: 203
35. Sun C. Q., Zhong W. H., Li S., Tay B. K., Bi H. L., and Jiang E. Y., J. Phys. Chem. B, 2004, 108: 1080
36. Tang Z. X., Sorensen C. M., Klabunde K. J., and Hadjipanayis G. C., Phys. Rev. Lett., 1991, 67: 3602
37. Weschke E., Ott H., Schierle E., Schűßler-Langeheine C., Vyalikh D. V., Kaindl G., Leiner V., Ay M., Schmitte T., and Zabel H., Phys. Rev. Lett., 2004, 93: 157204
38. Ambrose T. and Chien C. L., Phys. Rev. Lett., 1996, 76: 1743
39. Tang Y. J., Smith D. J., Zink B. L., Hellman F., and Berkowitz A. E., Phys. Rev. B, 2003, 67: 054408
40. Abarra E. N., Takano K., Hellman F., and Berkowitz A. E., Phys. Rev. Lett., 1996, 77: 3451
41. van der Zaag P. J., Ijiri Y., Borchers J. A., Feiner L. F., Wolf R. M., Gaines J. M., Erwin R. W., and Verheijen M. A., Phys. Rev. Lett., 2000, 84: 6102
42. Alders D., Tjeng L. H., Voogt F. C., Hibma T., Sawatzky G. A., Chen C. T., Vogel J., Sacchi M., and Iacobucci S., Phys. Rev. B, 1998, 57: 11623
43. Punnoose A., Magnone H., Seehra M. S., and Bonevich J., Phys. Rev. B, 2001, 64: 174420
44. Punnoose A. and Seehra M. S., J. Appl. Phys., 2002, 91: 7766
45. Stewart S. J., Multigner M., Marco J. F., Berry F. J., Hemando A., and Gonzalez J. M., Solid State Commun., 2004 130: 247
46. Zheng X. G., Xu C. N., Nishikubo K., Nishiyama K., Higemoto W., Moon W. J., Tanaka E., and Otabe E. S., Phys. Rev. B, 2005, 72: 014464
47. Fullerton E. E., Riggs K. T., Sowers C. H., and Bader S. D., Phys. Rev. Lett., 1995, 75: 330
48. Fisher M. E. and Barber M. N., Phys. Rev. Lett., 1972, 28: 1516
49. Zhang R. J. and Willis R. F., Phys. Rev. Lett., 2001, 86: 2665
50. Nikolaev V. I. and Shipilin A. M., Phys. Solid State, 2003, 45: 1079
51. Yang C. C. and Jiang Q., Acta Mater., 2005, 53: 3305
52. Meiklejohn W. H. and Bean C. P., Phys. Rev., 1956, 102: 1413
53. Nogués J. and Schuller I. S., J. Magn. Magn. Mater., 1999, 192: 203
54. Berkowitz A. E. and Takano K., J. Magn. Magn. Mater., 1999, 200: 552
55. Kiwi M., J. Magn. Magn. Mater., 2001, 234: 584
56. van der Zaag P. J., Ball A. R., Feiner L. F., Wolf R. M., and van der Heijden P. A. A., J. Appl. Phys., 1996, 79: 5103
57. Ijiri Y., Borchers J. A., Erwin R. W., Lee S. H., van der Zaag P. J., and Wolf R. M., Phys. Rev. Lett., 1998, 80: 608
58. Devasahayam A. J. and Kryder M. H., J. Appl. Phys., 1999, 85: 5519
59. Baltz V., Sort J., Landis S., Rodmacq B., and Dieny B., Phys. Rev. Lett., 2005, 94: 117201
60. Xi H. W., White R. M., Gao Z., and Mao S. N., J. Appl. Phys., 2002, 92: 4828
61. Fuke H. N., Saito K., Yoshikawa M., Iwasaki H., and Sahashi M., Appl. Phys. Lett., 1999, 75: 3680
62. van Driel J., de Boer F. R., Lenssen K. M. H., and Coehoorn R., J. Appl. Phys., 2000, 88: 975
63. Sang H., Du Y. W., and Chien C. L., J. Appl. Phys., 1999, 85: 4931
64. Rickart M., Guedes A., Ventura J., Sousa J. B., and Freitas P. P., J. Appl. Phys., 2005, 97: 10K110
65. Lund M. S., Macedo W. A. A., Liu K., Nogués J., Schuller I. K., and Leighton C., Phys. Rev. B, 2002, 66: 054422
66. Fulcomer E. and Charap S. H., J. Appl. Phys., 1972, 43: 4190
67. Xi H. W. and White R. M., J. Appl. Phys., 2003, 94: 5850
68. Ambrose T. and Chien C. L., J. Appl. Phys., 1996, 79: 5920
69. Valasek J., Phys. Rev., 1921, 17: 475
70. Mitsui T., Tatsuzaki I., and Nakamura E., An Introduction to the Physics of Ferroelectrics, New York: Gordon and Breach, 1976
71. Shaw T. M., Trolier-McKinstry S., and McIntyre P. C., Annu. Rev. Mater. Sci., 2000, 30: 263
72. Fong D. D., Stephenson G. B., Streiffer S. K., Eastman J. A., Auciello O., Fuoss P. H., and Thompson C., Science, 2004, 304:1650
73. Buscaglia M. T., Buscaglia V., Viviani M., Petzelt J., Savinov M., Mitoseriu L., Testino A., Nanni P., Harnagea C., Zhao Z., and Nygren M., Nanotechnology, 2004, 15: 1113
74. Chattopadhyay S., Ayyub P., Palkar V. R., and M. Multani, Phys. Rev. B, 1995, 52: 13177
75. Fu H. X. and Bellaiche L., Phys. Rev. Lett., 2003, 91: 257601
76. Ishikawa K., Yoshikawa K., and Okada N., Phys. Rev. B, 1988, 37: 5852
77. Lichtensteiger C., Triscone J. M., Junquera J., and Ghosez P., Phys. Rev. Lett., 2005, 94: 047603
78. Streiffer S. K., Eastman J. A., Fong D. D., Thompson G., Munkholm A., Ramana Murty M. V., Auciello O., Bai G. R., and Stephenson G. B., Phys. Rev. Lett., 2002, 89: 67601
79. Strukov B. A., Davitadze S. T., Kravchun S. N.. Taraskin S. A., Goltzman M., Lemanov V. V., and Shulman S. G., J. Phys.: Condens. Matter, 2003, 15: 4331
80. Wang Y. G., Zhong W. L., and Zhang P. L., Phys. Rev. B, 1996, 53: 11439
81. Zhao Z., Buscaglia V., Viviani M., Buscaglia M. T., Mitoseriu L., Testino A., Nygren M., Johnsson M., and Nanni P., Phys. Rev. B, 2004, 70: 024107
82. Zhong W. L., Jiang B., Zhang P. L., Ma J. M., Cheng H. M., Yang Z. H., and Li L. X., J. Phys.: Condens. Matter, 1993, 5: 2619
83. Spanier J. E., Kolpak A. M., Urban J. J., Grinberg I., Ouyang L.,

Yun W. S., Rappe A. M., and Park H. K., Nano Lett., 2006, 6: 735
84. Abe K. and Komatsu S., J. Appl. Phys., 1995, 77: 6461
85. Pertsev N. A., Zembilgotov A. G., and Tagantsev A. K., Phys. Rev. Lett., 1998, 80: 1988
86. Wang B. and Woo C. H., Acta Mater., 2004, 52: 5639; J. Appl. Phys., 2005, 97: 84109
87. Yano Y., Lijima K., Daitoh Y., Terashima T., Bando Y., Watanabe Y., Kasatani H., and Terauchi H., J. Appl. Phys., 1994, 76: 7833
88. Pertsev N. A., Tagantsev A. K., and Setter N., Phys. Rev. B, 2000, 61: R825
89. Zhang J., Yin Z., Zhang M. S., and Scott J. F., Solid State Commun., 2001, 118: 241
90. Sy H. K., J. Phys.: Condes. Matter, 1993, 5: 1213
91. Wang C. L., Zhong W. L., and Zhang P. L., J. Phys.: Condens. Matter, 1992, 4: 4743
92. Zhong W. L., Wang Y. G., Zhang P. L., and Qu B. D., Phys. Rev. B, 1994, 50: 698
93. Jiang Q., Cui X. F., and Zhao M., Appl. Phys. A, 2004, 78: 703
94. Bardeen J., Cooper L.N., and Schriepper J. R., Phys. Rev., 1957, 108: 1175
95. Ueda K. and Naito M., J. Appl. Phys., 2003, 93: 2113
96. Pogrebnyakov A. V., Redwing J. M., Jones J. E., Xi X. X., Xu S. Y., Li Q., Vaithyanathan V., and Schlom D. G., Appl. Phys. Lett., 2003, 82: 4319
97. Banerjee R., Vasa P., Thompson G. B, Fraser H. L., and Ayyub P., Solid State Commun., 2003, 127: 349
98. Strongin M., Thompson R. S., Kammerer O. F., and Crow J. E., Phys. Rev. B, 1970, 1: 1078
99. Ekinci K. L. and Valler Jr J. M., Phys. Rev. Lett., 1999, 82: 1518
100. Tsai A. P., Chandrasekhar N., and Chattopadhyay K., Appl. Phys. Lett., 1999, 75: 1527
101. Li W. H., Yang C. C., Tsao F. C., and Lee K. C., Phys. Rev. B, 2003, 68: 184507
102. Ido M., J. Phys. Soc. Jpn., 1976, 41: 412
103. Halperin W. P., Rev. Mod. Phys., 1986, 58: 533
104. Mühlschlegel B., Scalapino D. J., and Denton R., Phys. Rev. B, 1972, 6: 1767
105. Parmenter R. H., Phys. Rev., 1968, 166: 392
106. Abeles B., Cohen R. W., and Cullen G. W., Phys. Rev. Lett., 1966, 17: 632
107. Cantor B., Novel Nanocrystalline Alloys and Magnetic Nanomaterials, Bristol and Philadelphia: Instit. Phys. Publishing, 2005
108. Jiang Q., Tong H.Y., Hsu D.T., Okuyama K., and Shi F. G., Thin Solid Films, 1998, 312: 357
109. Hoshino K. and Shimamura S., Phil. Mag. A, 1979, 40: 137
110. Dash J. G., Rev. Mod. Phys., 1999, 71: 1737
111. Childress J. R., Chien C. L., Zhou M. Y., and Sheng P., Phys. Rev. B, 1991, 44: 11689
112. Jiang Q., Aya N., and Shi F. G., Appl. Phys. A, 1997, 64: 627
113. Jiang Q., Shi H. X., and Zhao M., J. Chem. Phys., 1999, 111: 2176
114. Regel′ A. R. and Glazov V. M., Semiconductors, 1995, 29: 405
115. Tiwari G. P., Juneja J. M., and Iijima Y., J. Mater. Sci., 2004, 39: 1535
116. Buckwald R. A., Hirsch A. A., Cabib D., and Callen E., Phys. Rev. Lett., 1975, 35: 878
117. Jiang Q., Zhang S., and Zhao M., Mater. Chem. Phys., 2003, 82: 225
118. Yang C. C., Xiao M. X., Li W., and Jiang Q., Solid State Commun., 2006, 139: 148
119. Zhang Z., Zhao M., and Jiang Q., Semicond. Sci. Technol., 2001, 16: L33
120. Lai S. L., Carlsson J. R. A., and Allen L. H., Appl. Phys. Lett., 1998, 72: 1098
121. Zhao M. and Jiang Q., Solid State Commun., 2004, 130: 37
122. Hou M., Azzaoui M. E., Pattyn H., Verheyden J., Koops G., and Zhang G., Phys. Rev. B, 2000, 62: 5117
123. Herr U., Jing J., Birringer R., Gonser U., and Gleiter H., Appl. Phys. Lett., 1987, 50: 472
124. Zhou M. Y. and Sheng P., Phys. Rev. B, 1991, 43: 3460
125. Childress J. R., Chien C. L., Zhou M. Y., and Sheng P., Phys. Rev. B, 1991, 44: 11689
126. Koops G. E. J., Pattyn H., Vantomme A., Nauwelaerts S., and Venegas R., Phys. Rev. B, 2004, 70: 235410
127. Zhao Y. H. and Lu K., Phys. Rev. B, 1997, 56: 14330
128. Kiguchi M., Yokoyama T., Matsumura D., Kondoh H., Endo O., and Ohta T., Phys. Rev. B, 2000, 61: 14020
129. Hou M., Azzaoui M. E., Pattyn H., Verheyden J., Koops G., and Zhang G., Phys. Rev. B, 2000, 62: 5117
130. Kastle G., Boyen H. G., Schroder A., Plett A., and Ziemann P., Phys. Rev. B, 2004, 70: 165414
131. http://www.webelements.com/
132. Lang X. Y., Zheng W. T., and Jiang Q., Phys. Rev. B, 2006, 73: 224444
133. Aguilera-Granja F. and Morán-López J. L., Solid State Commun., 1990, 74: 155
134. Jiang Q. and Lang X. Y., Macromol. Rapid Commun., 2004, 25: 825
135. Johnson D., Perera P., and O`Shea M. J., J. Appl. Phys., 1996, 79: 5299
136. Lang X. Y. and Jiang Q., Solid State Commun., 2005, 134: 797
137. van Vleck J. H., Rev. Mod. Phys., 1945, 17: 27
138. Mauri D., Siegmann H. C., Bagus P. S., and Kay E., J. Appl. Phys., 1987, 62: 3047
139. Kittel C., Rev. Mod. Phys., 1949, 21: 541
140. Malozemoff A. P., Phys. Rev. B, 1987, 35: 3679
141. Ali M., Marrows C. H., Al-Jawad M., Hickey B. J., Misra A., Nowak U., and Usadel K. D., Phys. Rev. B, 2003, 68: 214420
142. Lang X. Y., Zheng W. T., and Jiang Q., Nanotechnology, 2007, 18: 155701
143. Jungblut R., Coehoorn R., Johnson M. T., and J. aan de Stegge, Reinders A., J. Appl. Phys., 1994, 75: 6659
144. Wedler G. and Schneck H., Thin Solid Films, 1977, 47: 147
145. Scholl A., Liberati M., Arenbolz E., Ohldag H., and Sthör J., Phys. Rev. Lett., 2004, 92: 247201
146. Ou J. T., Wang F. R., and Lin D. L., Phys. Rev. E, 1997, 56: 2805
147. Cohen R. E., Nature, 1992, 358: 136
148. Kretschmer R. and Binder K., Phys. Rev. B, 1979, 20: 1065
149. Zembilgotov A. G., Pertsev N. A., Kohlstedt H., and Waser R., J. Appl. Phys., 2002, 91: 2247
150. Rarnesh R. and Schlom D. G., Science, 2002, 296, 19756
151. Lang X. Y. and Jiang Q., J. Nanopart. Res., 2007, 9: 595
152. Li Y. L., Hu S. Y., Liu Z. K., and Chen L. Q., Appl. Phys. Lett., 2001, 78: 3878

153. Jr G. A. Rossetti, Cross L. E., and Kushida K., Appl. Phys. Lett., 1991, 59: 2524
154. Speck J. S. and Pompe W., J. Appl. Phys., 1994, 76: 466
155. Lines M. E., Phys. Rev., 1969, 177: 797; Phys. Rev., 1969, 177: 812; Phys. Rev., 1969: 177: 819
156. Abrahams S. C., Kurtz S. K., and Jamieson P. B., Phys. Rev., 1968, 172: 551
157. Kim D. J., Jo J. Y., Kim Y. S., Chang Y. J., Lee J. S., Yoon J. G., Song T. K., and Noh T. W., Phys. Rev. Lett., 2005, 95: 237602
158. Junquera J. and Ghosez P., Nature, 2003, 422: 506
159. Spanier J. E., Kolpak A. M., Urban J. J., Grinberg I., Ouyang L., Yun W. S, Rappe A. M., and Park H. K., Nano Lett., 2006, 6: 735
160. Kreisel J. and Glazer A. M., J. Phys.: Condens. Matter, 2000, 12: 9689
161. Abe K. and Komatsu S., J. Appl. Phys., 1995, 77: 6461
162. McMillan W. L., Phys. Rev., 1968, 167: 331
163. Magomedov M. N., Phys. Solid State, 2003, 45: 1159
164. Pettit R. B.. Silcox J., Phys. Rev. B, 1976, 13: 2865
165. Weast R. C., Astle M. J., and Beyer W. H., CRC Handbook of Chemistry and Physics, 69th ed., CRC Press, Boca Raton, 1988: E95–F174
166. Vossloh C., Holdenried M., and Micklitz H., Phys. Rev. B, 1998, 58: 12422
167. Black C. T., Ralph D. C., and Tinkham M., Phys. Rev. Lett., 1996, 76: 688
168. Ralph D. C., Black C. T., and Tinkham M., Phys. Rev. Lett., 1997, 78: 4087
169. von Delft J., Zaikin A. D., Golubev D. S., and Tichy W., Phys. Rev. Lett., 1996, 77: 3189
170. Braun F. and von Delft J., Phys. Rev. B, 1999, 59: 9527